Neutral strange particle production at top SPS energy measured by the CERES experiment

---

Vom Fachbereich Physik
der Technischen Universität Darmstadt

zur Erlangung des Grades
eines Doktors der Naturwissenschaften
(Dr. rer. nat.)

genehmigte Dissertation von
Sylwester Radomski
aus Otwock

Referent: Prof. Dr. P. Braun-Munzinger
Koreferent: Prof. Dr. / Dr. h.c. (RUS) D.H.H. Hoffmann

Tag der Einreichung: 13. Mai 2006
Tag der Prüfung: 05. Juli 2006

Darmstadt 2006
D17

Summary

Systematics of strange particle production in collisions of ultrarelativistic nuclei provides an insight into the properties of the strongly interacting matter. Hadrochemistry, the study of the relative yields, provides information about chemical freeze-out and the position of the system in the phase diagram.

Strangeness production at Super Proton Synchrotron (SPS) energies is not fully explained by the thermal model of hadron gas. Data reported by one experiment show sharp structures as a function of energy which are interpreted as a signature for a phase transition, but due to discrepancies in the results between two different experiments, a conclusion can not be drawn.

This thesis is part of an effort to build a database of the strangeness production at SPS energy. The particular subject of this work is a precise measurement of the production of K^0_S. The results are compared with two other experiments and the prediction of the thermal model. The high precision data shed light on the systematics of strangeness production and allow clarification of the experimental status.

The study of transverse momentum spectra provides information about the temperature and the radial expansion of the system. Here, as in the case of particle yields, interesting structures are visible as a function of energy. A rapid increase in the number of degrees of freedom is visible in the SPS region.

A large part of the strangeness is carried by the neutral strange baryon Λ. Here the experimental situation is even more complicated because the reconstruction of the Λ yield requires large extrapolation to low transverse momentum. In this work first results on Λ production will be presented.

Zusammenfassung

Die Systematik der Produktion seltsamer Teilchen in ultrarelativistischen Schwerionenkollisionen eröffnet Einblicke in die Eigenschaften stark wechsel wirkender Materie. Hadrochemie, das Studium der relativen Häufigkeiten verschiedener Teilchen, liefert Informationen über den chemischen Freezeout und erlaubt es, das System in das Phasendiagramm der Kernmaterie einzuordnen.

Strangeness-Produktion bei SPS-Energien folgt nicht strikt den Voraussagen für ein thermisches Hadronengas. Die Daten weisen in ihrer Abhängigkeit von der Kollisionsenergie ausgeprägte Strukturen auf, die unter anderem als Signatur für einen Phasenübergang gewertet werden. Allerdings wird die Interpretation durch Diskrepanzen zwischen Messungen verschiedener Experimente erschwert.

Diese Arbeit gliedert sich in die gegenwärtigen Anstrengungen zum Aufbau einer Datenbank der Strangeness-Produktion bei SPS-Energien ein. Insbesondere wird die Produktion neutraler Kaonen K^0_S präzise bestimmt. Ein Vergleich unserer Resultate zu anderen Experimenten sowie dem thermischen Modell der Hadronenproduktion wird angestellt. Die hohe Präzision der Messung trägt signifikant zur Klärung der Datenlage bei und führt zu einem besseren systematischen Verständnis der Teilchenproduktion.

Anhand der Transversalimpulsspektren lassen sich Informationen über die Temperatur und radiale Expansion des Systems gewinnen. Ähnlich wie im Fall der Teilchenausbeuten sind in der Energieabhängigkeit ausgeprägte Strukturen erkennbar.

Das elektrisch neutrale seltsame Baryon Λ hat einen bedeutenden Anteil am gesamten Strangenessvorkommen. Da eine Bestimmung der absoluten Häufigkeit der produzierten Λ-Baryonen nur nach Extrapolation der Transversalimpulsspektren über einen weiten Bereich kleiner Impulse möglich ist, ist hier die experimentelle Situation noch komplizierter. In dieser Arbeit werden vorläufige Ergebnisse zur Produktion von Λ-Baryonen präsentiert.

Contents

1 Strangeness production in relativistic heavy ion collisions

Collisions of relativistic nuclei provide a unique opportunity to study strongly interacting matter. When two nuclei collide, some of their constituents, quarks and gluons, undergo collisions and longitudinal momentum is transfered into transverse momentum. A fireball of new quarks and gluons is created as a result of the collision. The partons in the fireball expand, rescatter and finally freeze-out. Hadronic remnants of the collision are accessible for detection. The freeze-out proceeds in two steps. At chemical freeze-out, when inelastic collisions stop the particle species are fixed, at kinetic freeze-out the elastic collisions stop and the momentum spectrum is established.

The energy density ϵ achieved during the collision, at midrapidity, can be estimated from the transverse energy of the produced particles according to the Bjorken formula [1]:

$$\epsilon = \frac{1}{\pi R^2 \tau} \frac{dN}{dy} \langle E_T \rangle \tag{1.1}$$

where πR^2 is the area in the transverse plane, τ is the formation time, dN/dy is the density of particles with mean transverse energy per particle $\langle E_T \rangle$. The formation time can not be measured experimentally, it is estimated to by $\tau \sim 1$ fm/c. The energy densities estimated using Eq. 1.1, at top SPS energy reach the values of $\epsilon \sim 1 - 4$ GeV/fm^3 from peripheral to central collisions [2].

As speculated in Ref. [3, 4], at these energy densities a new state of matter is formed. The quarks are not confined in hadrons but are dissolved and can move freely in the Quark Gluon Plasma (QGP). The search for the QGP and its properties is the central goal in the ultrarelativistic heavy ion collisions program.

1.1 Models of heavy ion collisions

There are two groups of theoretical frameworks to understand and describe the particle production during heavy ion collisions. The first group is based on microscopic description of the system, the second assumes thermalization. Theoretical frameworks based on

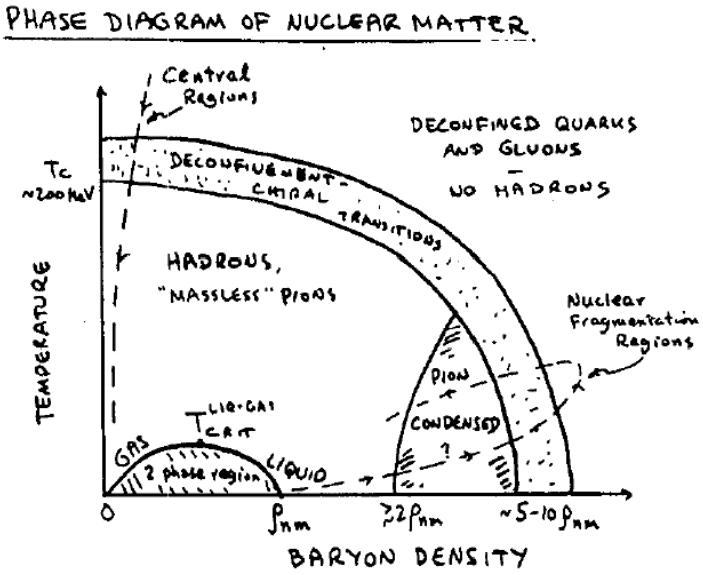

Figure 1.1: Historical plot (1983) of phase diagram of the nuclear matter in equilibrium and how it can be explored by ultra–relativistic heavy ions collisions [6]. For current version see Fig. 1.2.

microscopic description, for example UrQMD [5] are conceptually more elegant and give a result derived from first principles. These models provide a good description of data at low energies, but do not reproduce experimental data at SPS energies. Strangeness production and in particular the production of multi-strange particles at SPS energies is not properly described by UrQMD.

One can assume that during the collision the full thermalization takes place. In fact the formation of the Quark Gluon Plasma requires nuclear matter at equilibrium. In this approach the particle yields are not determined by the cross-sections for the particular processes, as in the microscopic models, but by the equilibrium conditions. The nuclear matter in equilibrium can be described by the external parameters – temperature, baryonic chemical potential and the volume. The phase diagram of the nuclear matter is shown in Fig 1.1. The properties of the phase diagram presented in this historical sketch were studied in detail over the last 30 years using both theoretical and experimental methods.

Theoretically the phase diagram can be studied using Lattice Quantum Chromodynamics (LQCD). LQCD predicts [7] that at sufficiently high temperatures the relevant degrees of freedom are not hadrons but quarks and gluons. The predicted temperature for the transition is around $T \simeq 170$ MeV at low baryochemical potential. The recent results show the transition is a crossover type at low baryochemical potential and after the critical point

the transition is of the first order.

The experimental program was started with the fixed target experiments at Bevalac and SIS accelerators with beam energies up to $E = 2$ GeV per nucleon. The Alternating Gradient Synchrotron (AGS) at Brookhaven National Laboratory (BNL) was operated with gold beams at momenta up to 11.5 GeV/c per nucleon. The next in the energy order is Super Proton Synchrotron (SPS) providing lead beams with momenta of 20, 30, 40, 80 and 158 GeV/c per nucleon. The accelerator started operating with the highest beam energy and only at the end of the heavy ion program was the energy scan performed.

The operation of the Relativistic Heavy Ion Collider (RHIC) at BNL in the year 2000 with beams of 130 GeV and later with 200 GeV started the era of the collider heavy ion experiments. The major discovery was the fact that particle production smoothly follows the systematics established at SPS. The future of the experimental program lies in the Large Hadron Collider (LHC) to start operating in the year 2007 with the ALICE experiment currently under construction.

In this work the beam energy always means the energy per nucleon and this term will be omitted. In the literature the energy ranges are often referred by the name of the facility not by the value. For example the momentum of 158 GeV/c is called top SPS energy.

Experimentally, the temperature and the baryonic chemical potential are not directly measurable; what can be measured are the particle yields and spectra. To place a point in the phase diagram using experimental data a thermal model, describing the yields by thermal parameters, is needed [11, 9] .

The strange particles are of special interest for extracting the thermal parameters of the system created. This is connected with the fact that their yields vary significantly in the SPS energy range, and, as will be demonstrated later, this variation is not fully understood. In addition, since the incoming nuclei do not carry any strangeness, all strange particles are produced during the collision.

In the thermal model the particle abundance is dominated by the mass to temperature ratio. The strange particles span a convenient mass range from $m \simeq 0.5$ GeV/c^2 (kaons) to $m \simeq 1.7$ GeV/c^2 for Ω^-, significantly above the freeze-out temperature.

1.2 Particle yields

The thermal model provides a method for extracting the thermal parameters of the studied system from the particle yields. The result of the analysis of a large data sample is shown on the left panel of Fig. 1.2. The experimental results are overlaid with the results from

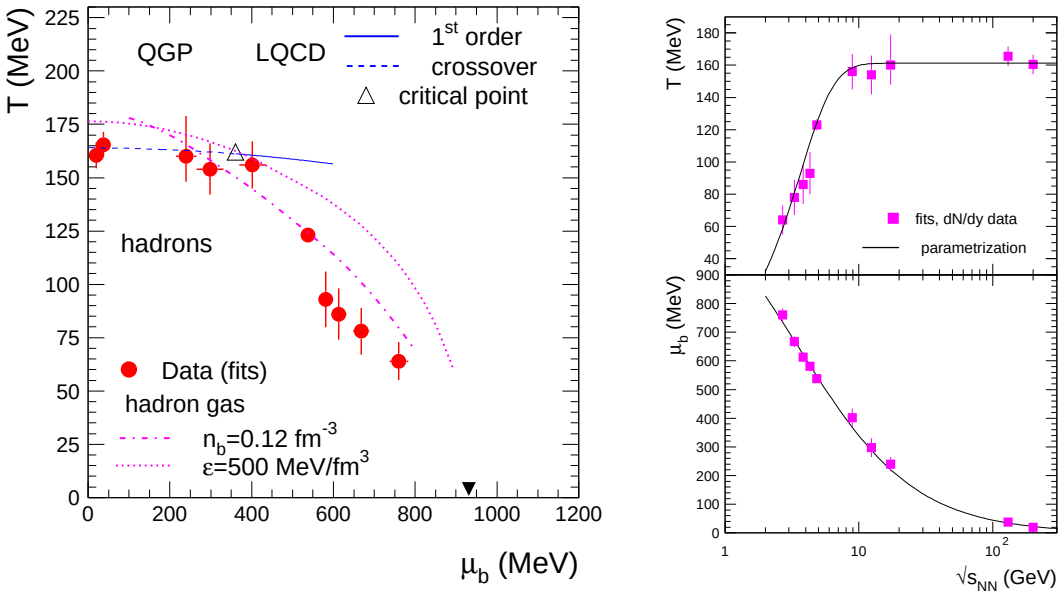

Figure 1.2: Left: phase diagram of nuclear matter studied by LQCD and the experiments. Right: energy dependence of the temperature and the baryochemical potential. Plots from Ref. [9].

LQCD and phenomenological curves of constant energy and baryon density. This plot shows the same as the sketch in Fig. 1.1, the experimental points follow the systematics of early predictions.

When following the experimental points starting from high baryochemical potential (low beam energies) toward high temperature (high beam energies), a smooth trend is observed. In the AGS energy regime a steep decrease in the baryochemical potential and a steep increase in temperature is observed. This trend changes at SPS energies. The temperature does not increase any more only the decrease of the baryonic chemical potential is observed. The detailed analysis of temperature and baryonic potential shown in the right panel of Fig. 1.2 shows that the temperature saturation point is located at about $\sqrt{s} = 8 - 9$ GeV, in the SPS energy range.

The maximum freeze-out temperature reached by the system created during the collision of nuclei is compatible with the temperature of the phase transition from a hadronic system to quark-gluon plasma obtained with lattice results. Also the saturation point coincides with the expected critical point. The conclusion that can be drawn from the above plot is that the energy range needed to study the onset of deconfinement is the SPS domain.

Some light can be shed on the origin of the coincidence of two temperatures – of deconfinement and of chemical equilibrium – by analysis of the process driving the system toward equilibrium. As speculated in Ref. [10], the two-particle interactions are insufficient to drive the system into chemical equilibrium or to maintain it. The reactions responsible for the equilibration are the multi-particle interactions, which require high density available only at the instant, or shortly after hadronization.

The thermal model describes particle production in the wide range of the collision energies starting from $\sqrt{s} = 2$ GeV up to $\sqrt{s} = 200$ GeV, the maximum energy available experimentally. The prediction power of the thermal model is illustrated in Fig. 1.3. The top RHIC energy is presented due to the largest number of the measurements performed by three independent experiments. Out of 18 ratios spanning three orders of magnitude almost all are described properly, within experimental error, by the thermal model with two parameters. The ratios not fully described involve the strongly decaying resonances.

The systematics of the particle ratios as a function of the collision energy is shown in Fig. 1.4. The shape of the excitation functions is correlated with the shape of the two excitation functions of temperature and baryochemical potential shown in right panel of Fig. 1.2. The proton to pion ratio follows the shape of μ_B. The K^-/π^- ratio shows the increase of the temperature. The shape of the K^+/π^+ ratio shows different behavior than K^-/π^-because the s quark can go into K^+ or Λ and thus the K^+/π^+ ratio is sensitive to temperature and baryochemical potential. The number of Λ/π is first driven

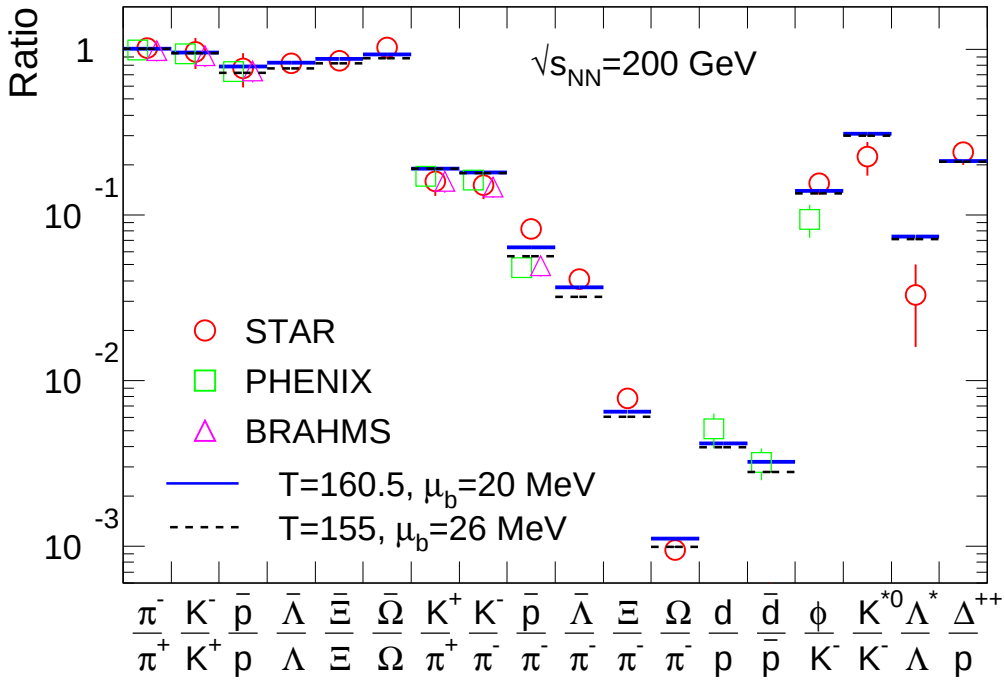

Figure 1.3: Particle ratios in data and thermal model at top RHIC energy. Good agreement between data and the thermal model is visible. Plot from Ref. [9]

up due to the increasing number of strange quarks and then falls due to the decreasing number of baryons. Some discrepancies between the thermal model and the experimental data are however visible in the strangeness sector at SPS, when the interplay between the temperature and baryochemical potential is dominating the shape.

The K^+/π^+ ratio shows a peak at the energy $\sqrt{s} = 7$ GeV, just before the freeze–out temperature saturates. The thermal model does not fully reproduce the shape of the excitation function from present data. The real discrepancy between the smooth thermal model prediction and a sharp peak would imply a new exciting physics beyond the thermal model – possibly giving a direct insight into the onset of deconfinement.

The so called "horn" structure was predicted in the Statistical Model of Early Thermalization (SMET) [12]. In this model the thermalization is achieved during the early hot stage and thus the number of strange particles is different than in the thermalization achieved or maintained in the hadronic phase at chemical freeze–out.

In this model two distinct phases and the mixed phase are explicitly part of the model thus a non-monotonic behavior is an obvious consequence. Since the model explores transition from the matter dominated by the incoming nuclei and the matter created during the collision, the horn appears in the same position as the bumps in Λ/π^+ and K^+/π^+.

The original plot with the prediction and data then available is shown in Fig. 1.5. The variables used in this plot are different from the ones used previously. The beam energy is expressed in Fermi-Landau energy F, which contain the threshold energy for the pion production. In the energy scales discussed here one can approximate $F = s^{1/4}$. The "horn" is located at $F \simeq 2.3$ GeV$^{0.5}$. The strangeness-to-entropy ratio E_S is experimentally approximated by:

$$E_s = \frac{< \Lambda > + < K + \overline{K} >}{< \pi >} \tag{1.2}$$

where $< \Lambda >$ stands for the sum of all hyperons (including Σ and multi-strange), $< K + \overline{K} >$ for the total sum of kaons and anti-kaons and $< \pi >$ is the total number of pions: π^+, π^- and π^0. As will be discussed in the last section of this chapter the number of $< K + \overline{K} >$ equals $4* < K^0_S >$, to account for K^+, K^-, K^0_S and K^0_L. This model offered a prediction for apparently sharp structures observed experimentally during the energy scan performed at lower SPS energies.

The discussion of possible sharp structures in systematics is however complicated by the fact that the strangeness production, in particular with the absolute normalization, is a difficult measurement. This is reflected in Fig. 1.4 by the points marked as closed and open symbols – values provided by different experiments. Pragmatically on can assume

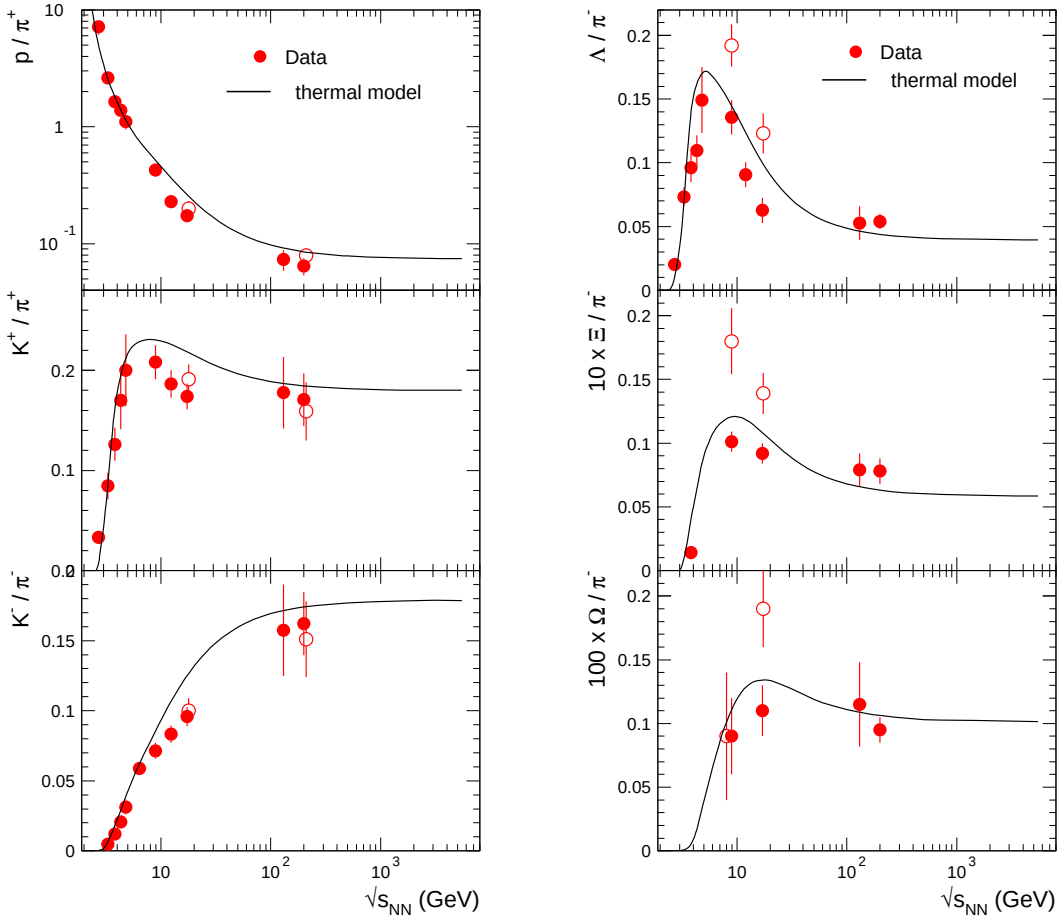

Figure 1.4: Particle ratios as a function of the energy in the center of mass. The black line represents prediction of the parametrized thermal model [9]. The points show experimental data. In the SPS region the full points show NA49 values while the open points show the NA44 values for charged kaons and the NA57 values for hyperons. Plot from Ref. [9].

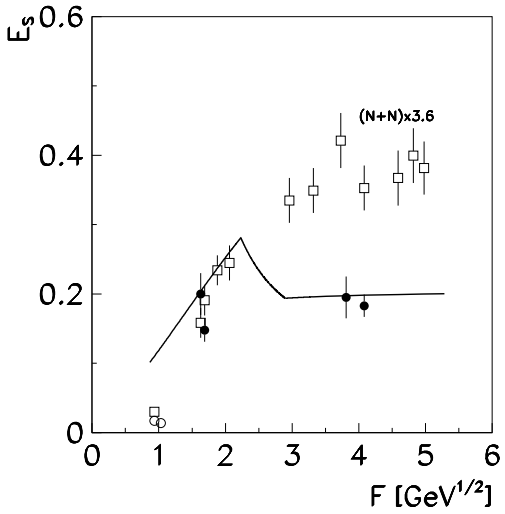

Figure 1.5: Prediction of the strangeness production systematics within the SMET, the plot is from Ref. [12]. Closed points: data from heavy ion experiments, open points: scaled nucleus–nucleus interactions. For definition of Fermi energy F and strangeness to entropy ratio E_s see text.

the systematic error of all data is equal to the discrepancy between the two independent measurements[1]. Based on this assumption no conclusion can be drawn with regard to the physics beyond the smooth thermal model.

The experimental data and its relation to the theoretical models generate an effort to build a database of strangeness production in heavy ion collisions at SPS energies and this thesis is part of this effort. In particular the discrepancy between mean number of charged kaons from NA49 and the K^0_S from NA57 will be addressed with the precisions measurement of K^0_S in CERES.

1.3 Transverse momentum spectra

Particle spectrum from which one can extract temperature is an additional source of information about the system created during heavy ion collisions. The temperature extracted from the transverse momentum spectrum reflects the conditions of the kinetic freeze-out in contrast to yield, which reflect the chemical freeze-out. In this area the strange particles are of special interest and the experimental results are interesting but inconclusive.

[1] More refined methods are used by the Particle Data Group to compile data, but they will not change the argument.

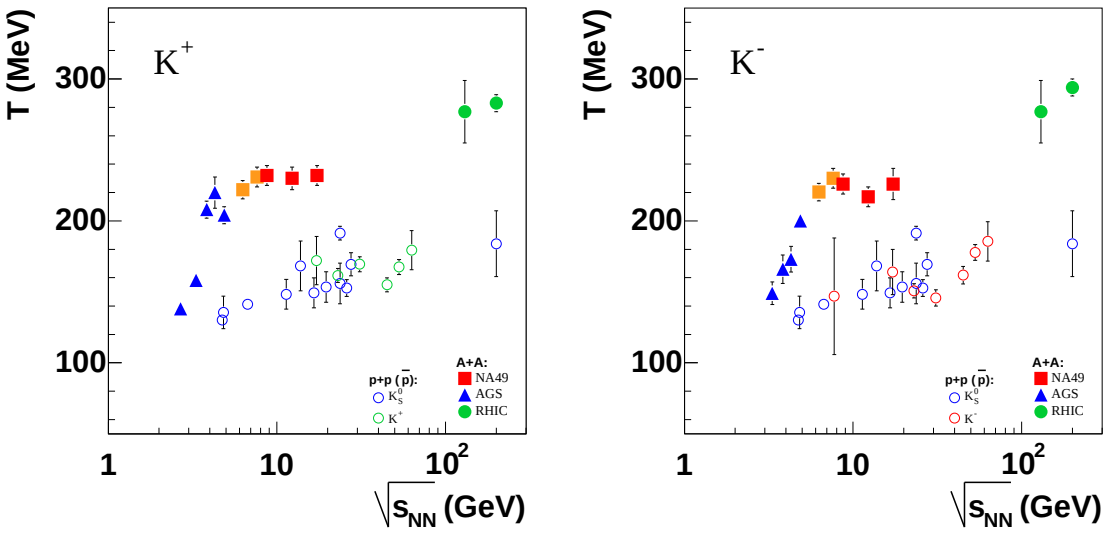

Figure 1.6: Temperature of charged kaons as a function of the collision energy. Closed symbols: heavy ion experiments, open symbols: nucleus–nucleus experiments. Plots from Ref. [13].

The temperature extracted from the slope of the transverse mass distribution is not the same as the temperature extracted from the thermal model. The former is greater due to expansion in radial direction, which also causes particles with different masses to have different apparent temperatures. In the literature three terms are used interchangeably: temperature, apparent temperature and inverse slope parameter. In this work the term temperature will be used even if the apparent temperature is more precise.

The best particles for the study of the temperature are kaons because they have an exponential transverse mass spectrum over a broad range of energies [13]. Pions are not exponential due to contributions from resonance decays, and the spectrum of heavy particles is distorted due to expansion. The exponential shape makes the measured temperature independent of the experimentally covered transverse momentum range.

The temperature of positive and negative kaons as a function of energy is shown in Fig. 1.6. The temperature increase with collision energy up to $T \simeq 220$ MeV and then at $\sqrt{s} = 10$ GeV the plateau sets in and the temperature increase slowly to $T = 280$ MeV at RHIC energies. One can also interpret these figures as a steep increase with energy followed by saturation with flat temperatures in the SPS range and later a slow increase toward RHIC energy. Comparing the latter interpretation with the phase diagram of boiling watter would suggest a phase transition and mixed phases at $\sqrt{s} = 8 - 20$ GeV. The statistical precision of data is not good enough to make such a strong statement. The new results on neutral kaons from NA57 at top SPS of $T = 234 \pm 9_{stat} \pm 23_{syst}$ MeV [45] would support

a smooth, slow increase but not a flat shoulder.

Also here, as for particle yields, no conclusive data set is currently available. What can be deduced from the data set is the increasing number of degrees of freedom at SPS energy. Whether this increase has a smooth or sharp structure can not be determined from current data. The precision measurement of the temperatures at top SPS energy and the measurements from the energy scan from RHIC will provide decisive data. The temperature obtained in this work will be discussed in Chapter 7.

1.4 Discrepancies of the experimental results

As discussed above, the measurement of the yields of strange particles is not an easy task. This is reflected in the discrepancies between experimental results obtained by different experiments. This section will discuss the issue of the experimental data discrepancy at top SPS energy.

1.4.1 The ϕ puzzle

The vector meson with hidden strangeness, the ϕ is a very interesting probe. This particle has decay channels into both hadrons and leptons. If it decays into leptons the decay products travel undisturbed toward the detector. If it decays into hadrons the decay products can rescatter. One can try to extract the properties of the rescattering stage [19]. It was also predicted that near the phase boundary, in dense medium, the mass, width and branching ratios into hadrons and leptons might be modified. This would produce an additional effect smaller than that proposed in the rescattering scenario.

Three experiments have measured ϕ production. The NA50 experiment measured ϕ mesons in the $\phi \rightarrow \mu^+\mu^-$ channel [20]. The measurement in the hadronic channel $\phi \rightarrow K^+K^-$ was obtained by NA49 [21] and recently CERES measured both hadronic ($\phi \rightarrow K^+K^-$) and leptonic ($\phi \rightarrow e^+e^-$) channels [19].

The transverse mass spectra from all experiments are shown in Fig 1.7. The discrepancy between decays into muons $\phi \rightarrow \mu\mu$ (NA50) and hadrons (NA49) in the overlapping transverse mass region is at the level of factor $2-4$. Also the transverse mass spectra slopes differ: 305 ± 15 MeV in the $\phi \rightarrow KK$ channel in NA49 and 218 ± 6 MeV in NA50.

Such a discrepancy is not observed when comparing the two channels measured by the CERES collaboration. The measured yields at the same rapidity are $2.05 \pm 0.14\,(stat) \pm 0.25\,(syst)$ in the hadronic channel and $2.04 \pm 0.4\,(stat) \pm 0.3\,(syst)$ in electrons. This measurement can exclude the enhancement of the ϕ yield in the leptonic channel greater

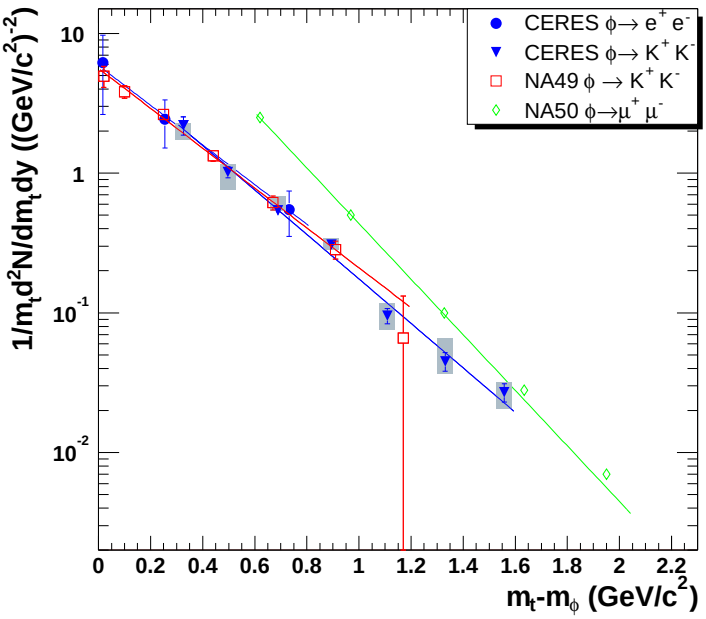

Figure 1.7: Transverse mass spectrum of ϕ mesons reconstructed in hadronic and leptonic channels at top SPS energy. Plot from Ref. [19].

than 1.6 at a confidence level of 95%. This result from the CERES experiment resolves the so-called "SPS ϕ puzzle".

1.4.2 Kaons and hyperons

A complete set of measurements of strange particles was obtained by two experiments: NA49 and NA57 (without ϕ). Both experiments operate detectors based on completely different approaches.

The NA49 experiment is based on four large Time Projection Chamber (TPC) detectors. Two vertex TPCs are immersed in a strong magnetic field. The charged kaons are identified using specific energy loss in TPCs. Additional π/K separation is done at midrapidity with a Time of Flight (TOF) detector. Hyperons and neutral kaons are measured by the reconstruction of the decay topology. This experiment have a large coverage in rapidity space.

The NA57 experiment is composed of silicon detectors (SD). An array of pixel detectors has a total length of about 30 cm. To improve momentum resolution additional double-sided silicon strip detectors are placed downstream of the telescope.

The results reported by NA49 and NA57 are collected in Table 1.1. The data are presented as values at midrapidity. The numerical values of the NA49 results are taken from the

hadron	NA49	NA57	difference
K^+	$29.6 \pm 0.3 \pm 1.5$		
K^-	$16.8 \pm 0.2 \pm 0.8$		
K^0_S	–	30.2 ± 2.2	30%
$0.5 * (K^+ + K^-)$	23.2 ± 0.5		
Λ	$11 \pm 1 \pm 1.3$	$18.5 \pm 1.1 \pm 1.8$	70%
$\bar{\Lambda}$	$1.54 \pm 0.16 \pm 0.2$	2.72 ± 0.2	76%
Ξ^-	1.61 ± 0.08	$2.08 \pm 0.09 \pm 0.21$	30%
Ξ^+	0.36 ± 0.04	$0.51 \pm 0.04 \pm 0.05$	40%
Ω	$0.19 \pm 0.03 \pm 0.01$	$0.39 \pm 0.04 \pm 0.06$	
$\bar{\Omega}$	$0.097 \pm 0.02 \pm 0.0$		

Table 1.1: Compilation of the results on strangeness from NA49 (first column) and NA57 (second column) at top SPS energy. Data obtained or scaled to 5% of geometrical cross-section. The first error is statistical and the second systematic. See text for source of data.

compilation [22], the original reference will be given when discussing a particular result. Data are for collisions with centrality of 5% of the geometrical cross-section. The weak signals, for example Ω^-, are measured with lower centrality and the results reported are scaled.

The results from NA57 are taken from [23]. Only data for the 5% most central collisions are shown, except for Ω, where the 10% centrality is reported. For K^0_S and $\overline{\Lambda}$, following the Gaussian distribution in the rapidity, the result of the fit at midrapidity is shown, for other particles following relatively flat distribution in the midrapidity region, the mean value is quoted:

$$\frac{dN}{dy}|_{y=0} = \int_{-0.5}^{0.5} dy \, \frac{dN}{dy} \tag{1.3}$$

where the integration spans one unit of rapidity and dN/dy are the measured points.

In all cases, the values reported by the NA57 are greater than those reported by NA49. The comparison of Λ and $\overline{\Lambda}$ gives the discrepancy at the level of 70%. Interestingly, the ratio $\overline{\Lambda}/\Lambda$ for both experiments is similar:

NA49 $\quad 1.54/11 = 0.14 \pm 0.01$

NA57 $\quad 2.72/18.5 = 0.147 \pm 0.01$

Also the systematics is similar as can be seen in Fig. 1.4, only the absolute scaling is different. This important aspect – the difference of absolute yields and the similarity of

the ratios imply, some systematic errors cancel when deriving the ratio. The difference in the absolute values can be caused by different centrality measures. This effect is important when discussing differences of $5-10\%$ of the yield. In the case of the particle to antiparticle ratio the value can be obtained using raw yields without any efficiency correction and fitting the transverse momentum spectrum. In this case the systematical uncertainty due to efficiency correction drops out.

The comparison of the K^0_S yield from NA57 to the mean of charged kaons gives a 30% discrepancy. The details of discrepancies for K^0_S will be discussed in greater detail after presentation of the results of neutral kaon reconstruction. The results presented here will help to understand the structures and sources of discrepancies.

1.5 Strange particles

The main subject of this thesis is the reconstruction of the neutral kaons K^0_S. Peculiar properties of this particle, which have a significant impact on the development of the Standard Model, will be discussed briefly in this section. For the interpretation of the results of this analysis only the isospin symmetry and the quark content of the K^0_S are important.

The strange particles can be divided into mesons and baryons. There are four mesons containing one strange and one light quark: $K^+ = |u\bar{s}\rangle$, $K^- = |\bar{u}s\rangle$, $K^0 = |d\bar{s}\rangle$ and $\overline{K^0} = |\bar{d}s\rangle$. Two of them K^- and $\overline{K^0}$ form an iso-doublet containing strange quark while K^+ and K^0 form an iso-doublet with anti-strange quark. There is also a vector meson with hidden strangeness $\phi = |s\bar{s}\rangle$.

The K^0 is not an antiparticle to itself, unlike for example π^0 or ϕ, its antiparticle is $\overline{K^0}$. This can be written with the help of the symmetry operator CP:

$$CP\left(K^0\right) = \overline{K^0}. \tag{1.4}$$

The two particles differ by two units of strangeness, but the strangeness is not conserved in the weak interactions and the neutral kaon can decay into two pions:

$$K^0 \to \pi^+\pi^- \tag{1.5}$$

and its antiparticle has the same decay products:

$$\bar{K^0} \to \pi^+\pi^-. \tag{1.6}$$

Since the two states can not be distinguished from the decay products the two states can oscillate:

$$K^0 \to \pi^+\pi^- \to \overline{K^0}. \tag{1.7}$$

If the CP symmetry holds, the particles having definite lifetime and actually observed are CP eigenstates. Two eigenstates are created:

$$K_1 = 1/\sqrt{2} * \left(K^0 + \overline{K^0}\right) \tag{1.8}$$

with the $CP = +1$ and

$$K_2 = 1/\sqrt{2} * \left(K^0 - \overline{K^0}\right) \tag{1.9}$$

with the $CP = -1$. The eigenstate with $CP = +1$ can decay into two pions, the second eigenstate with $CP = -1$ can decay into three pions. Since the mass of the neutral kaon is close to the mass of three pions, this decay mode has a smaller phase–space available and the decay proceeds slower than the decay of the $CP = +1$ eigenstate.

The two eigenstates have different lifetimes and thus are called "short" and "long". The short component K_S^0 equal to K_1 has $c\tau = 2.6842$ cm and the long component $K_L^0 = K_2$ has lifetime of $c\tau = 15.51$ m [14].

The K_S^0 is not exactly equal to K_1 due to the additional effect of the breaking of the CP symmetry observed first in the decay of $K_L^0 \to \pi\pi$ [15].

Historically, the K_S^0 was discovered first in the associated production with Λ. The analysis of the CP symmetry by Pais and Gell-Mann lead to the prediction of K_L^0 particle [16] which was experimentally discovered by a group lead by Ledermann [17, 18]. After discovery of the long component K_L^0 the regeneration of the short component of the beam of K_L^0 crossing the matter was discovered.

Detailed study of the suppression of decay into two muons, a signature of the fourth quark, and of the regeneration lead to the discovery of the decay of the K_L^0 into two pions [15], the decay forbidden by the CP symmetry. The breaking of the CP symmetry needed a third family of quarks. Thus the third quark was needed to explain the existence of K^0 and another three to explain its properties.

The important property of the neutral kaon is the mixing – the K_S^0 measure the number of both strange and anti-strange quarks. One also has to remember that the K_S^0 accounts for half of the total number of neutral kaons.

From the isospin symmetry the number of K^0 created shall be equal to the number of negative kaons and the number of $\overline{K^0}$ to the number of positive kaons. Summarizing, the number of K^0_S actually observed experimentally is equal to mean value of both charged kaons. The total number of kaons is $N = 4 * K^0_S$. This isospin argument holds up to the small effect of the feed-down from weak decays.

For a complete measurement of the number of strange quarks in the system the strange baryons also have to be reconstructed. Strange baryons can have one, two, or three strange or anti-strange quarks. One strange quark is contained in the iso-singlet Λ and in the iso-triplet Σ. Two strange quarks are in the iso-doublet Ξ and three strange quarks constitute Ω^-.

The total number of strange quarks carried by baryons is difficult to measure due to the Σ particle. The charged Σ particles decay weakly into one charged and one neutral particle, thus detection is impractical. The neutral Σ decays electromagnetically into

$$\Sigma^0 \rightarrow \Lambda\gamma \tag{1.10}$$

and thus a fraction of the measured Λ particles are feed–down from Σ^0. The measurement of the Σ^0/Λ ratio, using an electromagnetic calorimeter combined with the isospin symmetry would allow a measurement of the total number of strange particles carried by baryons.

1.6 Organization of the thesis

The main subject of this thesis is the reconstruction of the neutral strange meson K^0_S. The reconstruction procedure is divided into five parts covered in the subsequent chapters.

After a basic description of the experimental setup a feasibility study of the measurement is discussed. Different possibilities are studied and compared to other measurements addressing strangeness production in heavy ion collisions. The next chapter discusses the data analysis – creation of the invariant mass spectrum and approximation of the shape of the background. Selection of events and tracks as well as removal of the correlations other than K^0_S is extensively discussed in this chapter. Two types of correlations will be discussed: global correlations due to the impact parameter fluctuation and azimuthal flow, and localized ones – contamination from Λ decay.

The reconstruction efficiency was analyzed using a Monte-Carlo program and is the subject of Chapter 5. The result of this study will also provide the guidance for the choice of the details of the data treatment.

The final analysis addresses the issue of extracting the signal from the invariant mass spectrum and combining data with the results of simulations. This chapter will bring the first results with direct interpretation – transverse momentum and rapidity spectrum. The values obtained are compared to other measurement in Chapter 7.

Reconstruction of the neutral baryons is described shortly in Chapter 8. The reconstruction of Λ particle can be made using the same algorithms as K^0_S – thus only the important differences are discussed. The absolute measurement of neutral baryons is however difficult due to extrapolation of the transverse momentum spectrum and the substantial feed–down correction impossible to reconstruct in CERES setup. The results obtained will be briefly compared to other experiments.

The final chapter will give an overview the most significant conclusions from preceding chapters and summarize the results. In this chapter the interpretation of the results within the systematics of strange particles production will be given.

In this thesis a mixed unit system is used. The plots and numerical values follow the experimental tradition with the speed of light written explicitly. The formulae follow the theoretical tradition and the speed of light is omitted. The temperature is expressed in MeV.

2 The CERES experiment

The CERES/NA45 experiment was build for the study of di-lepton production in the intermediate mass region. Data from the first runs established the enhancement of the di-leptons in heavy ion induced reactions with respect to hadronic cocktail and reference p-Be collisions. For a recent review of the di-lepton results from data collected in 1995–1996 see Ref. [24].

In the original setup the momentum measurement was possible only for the electrons. With the installation of the radial TPC in 1998 and change of the magnetic field the CERES also became a hadron spectrometer. The CERES detectors have common acceptance in the polar angle of $8^0 < \theta_{lab} < 15^0$ and have full azimuthal coverage. The spectrometer covers a broad range of transverse momentum in the backward hemisphere.

2.1 Experimental setup

The CERES setup as operated during data taking in the fall of 2000 is shown in Fig. 2.1. The reactions were induced by a lead beam with momentum 158 GeV/c per nucleon, which gives center of mass energy of $\sqrt{s} = 17.3$ GeV.

The lead beam enters from the left side and hits a gold target segmented into 13 sub-targets. The gold disks are 25 μm thick and are separated by 2 mm. The geometry of the sub-targets is such that the secondaries within the acceptance do not cross the other targets. The segmentation of the target with the geometry explained above reduces the di-lepton background from conversions $\gamma \to e^+e^-$.

The central PbAu collisions are selected using a trigger consisting of three Beam Counters (BC) and the Multiplicity Counter (MC). Two counters, BC1 and BC2, are located before the target and BC3 is downstream of the target. The coincidence of two counters BC1 and BC2 gives the BEAM trigger. The disappearance of the beam particle – no signal in BC3 – indicates a nuclear reaction, the minimum bias trigger (MINB) is fired by BEAM trigger with anti-coincidence of BC3.

The centrality of the event can be approximated by the multiplicity measured by the Multiplicity Counter (MC). The signal from MC above the threshold with the MINB trigger

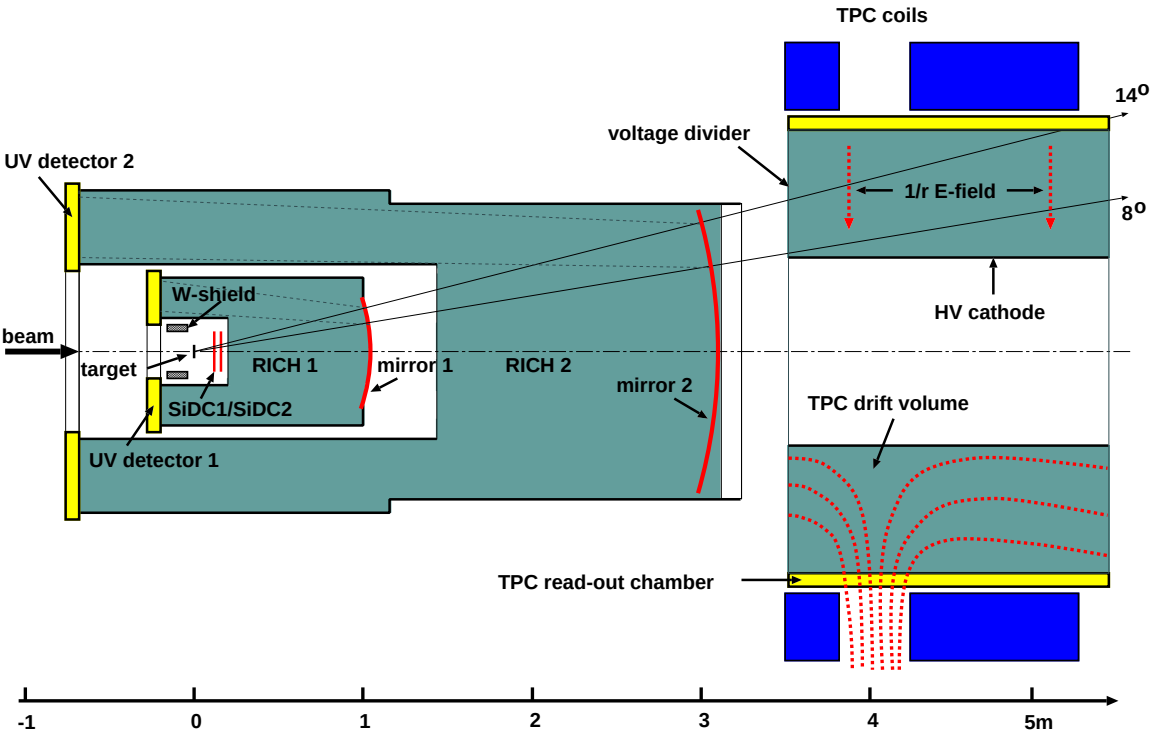

Figure 2.1: The CERES setup.

gives a trigger for the central events CENT. During data taking in 2000 the experimental program was concentrated on collecting a large number of central events. Minimum bias events and beam triggers were collected for the absolute calibration of the centrality and for multiplicity measurement.

The first detector registering the particles created during the collision is the silicon tracker (SD) composed of two layers of silicon drift detectors. Besides the tracking, the task of this detector is the reconstruction of the primary vertex. In this K^0_S analysis the information from SD was not used.

After SD the tracks cross two Ring Imaging Cherenkov (RICH) detectors. The Cherenkov light emitted by electrons and high momentum tracks in radiators is reflected by the mirrors and registered by the UV detectors located behind the target. Those detectors are the backbone of the old CERES setup and are the main device used to identify electrons. In this analysis, the data from RICH detectors will not be used.

The main tracking device in the CERES setup is the radial Time Projection Chamber (TPC) located 3.4 m downstream of the target. Before the TPC the particles run in a magnetic field-free region, the TPC is immersed in the push-pull magnetic field shifting the tracks in the azimuthal direction (phi-kick) depending on their momentum. The recon-

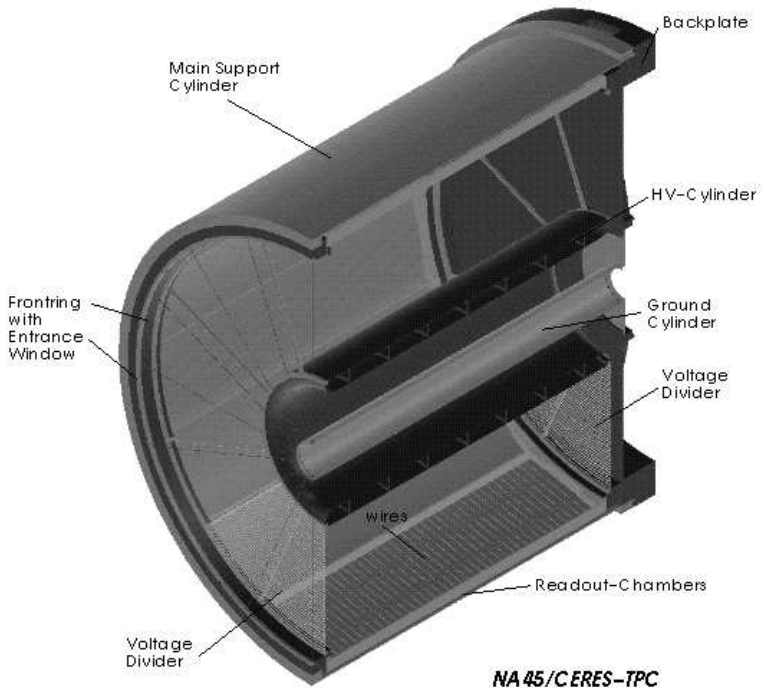

Figure 2.2: The CERES Time Projection Chamber.

struction of the deflection in the magnetic field allows the measurement of the momentum of the charged particle.

2.2 CERES TPC

The TPC is a three dimensional detector allowing track reconstruction and particle identification using specific energy loss dE/dX. The detector has a cylindrical shape and the active volume have the size of 9 m^3. The detector is sketched in Fig. 2.2.

When a charged particle travels in a gas, in this case a mixture of Ne/CO_2 in a proportion 80/20, it ionizes atoms. The energy loss depends on the momentum of the particle and is described by the Bethe–Bloch formula. The primary electrons travel along the electric field toward the outer shell of the cylinder where they trigger an avalanche. The generated signal is registered by the electronics located at the outer shell.

The TPC is segmented into 16 chambers in the azimuth. Each chamber has 20 rows in the beam direction and every row is segmented into 768 pads in azimuth. The third, radial coordinate is obtained using the arrival time of the ionization electron and is segmented into 256 bins. In total the number of electronic channels is a quarter of a million and the number of pixels including the time direction is 6×10^7.

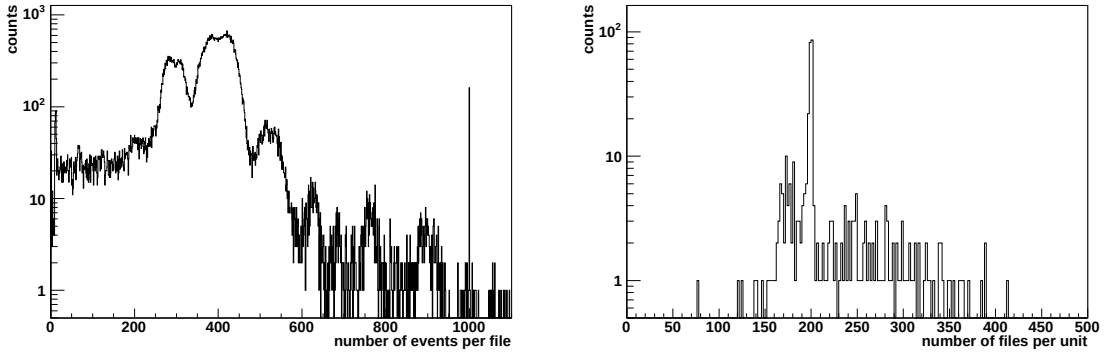

Figure 2.3: Left: number of events per burst. Right: number of files per calibration unit.

The track reconstruction algorithm is optimized for primary tracks. The tracking operates in the cylindrical coordinate system (ρ, ϕ, z) and the results are provided in the spherical momentum space (p, θ, ϕ).

The track is created from an array of subsequent hits in the beam direction and the tracks have a maximum of 20 hits. This value decreases at the border of acceptance. During the hit search in the (ρ, z) plane the track is required to be a straight line pointing at the primary vertex. In the azimuthal plane the location of the track's hits is predicted using templates generated with simulations.

The specific issues of the tracking performance relevant for the reconstruction of the weakly decaying secondary particles will be discussed in the chapter on data analysis.

2.3 Data processing

The data are organized in the following way. One file stores data obtained in one burst of the accelerator with typically around 400 events. The distribution of the number of events in a burst is presented in Fig. 2.3. The bursts with a higher number of events are from minimum bias runs. The bursts are organized in calibration units where every unit corresponds to one directory, a typical unit has 200 bursts. The number of files per unit is shown on right panel of Fig. 2.3. The calibration units are also used as packets of data for processing and analysis.

Data processing is a multi-step procedure. In the CERES collaboration these steps are numbered step0, step1, step2, step2+ and step3. The final production step3 is subdivided for the analysis of the charged tracks (step3c) and for the electrons (step3e). Currently, the physics analysis is performed using the step3 production.

total number of runs	521
total number of runs with 1 burst	51
total number of bursts (files)	106 666
total number of events	38 473 269
total amount of data accumulated	**18.5 TB**

Table 2.1: Summary of DAQ system performance

The output data structures of the step2 production contains events with the reconstructed tracks and the reconstructed hits belonging to tracks. Step2 can be used for the physics analysis but the size of total data sample is around 20 TB and is stored on tape robot at the CERN computing center. Processing the full sample requires a time consuming data staging from tape to disk.

The idea of step3 production is to perform a better calibration and reduce the size of data. The data compression was achieved mostly by the elimination of the space points from the TPC which was possible after careful calibration. The output structures contain only event information and tracks with the parameters with direct interpretation (eg. momentum). The total data size is around 3.6 TB. The reduction in size enables storing data directly on disks which eliminates tape staging time.

The momentum calibration is called step2+ and is based on the detailed analysis of the electric and magnetic fields inside the TPC. Additional checks are performed by reconstruction of the position of the Λ and $\overline{\Lambda}$ invariant mass peak. The details of the calibration are presented in Ref. [25]. The results of step2+ are used during the refitting of the tracks during step3 production.

Two step3c productions were created. This work used the second production step3c v2 performed on the CERN batch farm during August–October 2004. The output data, around 3.6 TB, was subsequently copied over the network to GSI and located on the disk servers. The servers were initially operated using NFS protocol. Due to low performance of the NFS protocol in the GSI environment the more basic SCP protocol was later employed. The results presented in this work were obtained on the GSI batch farm.

At every step of data processing additional information is stored into log files. Finally those files were uploaded into a relational database. The open source MySQL database server [26] was chosen for storage of the log information.

The summary of the DAQ performance is provided in Table 2.1. In total 38 million events were collected, including laser runs. The raw data collected by the experiment is 19 TB.

The step2 production was performed in three parts – *prod012*, *prod013* and *prod14*. this naming convention was used also in step3c. The production *prod012* contains data samples

production name	files in step2	events in step2	events in step3c
NULL	15 354	4 789 741	
prod012	61 069	23 633 311	23 165 212
prod013	28 936	9 389 304	8 613 575
prod014	1307	660 913	151 655

Table 2.2: Number of events and files in the step2 and step3c productions

with centrality $\sigma = 7\%$, the production *prod013* contains data samples with centrality $\sigma = 20\%$ and the data with the reversed magnetic field. The last production, *prod014*, contains special events including empty target. The number of files and events for every production is shown in Table 2.2. The production marked in table as NULL contains laser events and was processed in a different schema not discussed here. In this analysis productions *prod012* and *prod013* without the reversed field were used. This sample is contained in around 85 000 files.

3 Feasibility study of the strange meson production measurement in the CERES experiment

3.1 Methods of identification of the strange mesons

Charged strange mesons can be identified using three different signatures: specific energy loss dE/dX, identifying the kink from decay $K^+ \to \mu^+ + \nu$ or tree body decay $K^+ \to \pi^+\pi^+\pi^-$ called τ decay. Neutral strange meson K^0_S can be identified by decay into two particles $K^0_S \to \pi^+\pi^-$.

Each of the measurements requires different properties of a detector. The measurement using specific energy loss needs precise measurement of the ionization energy, which can be achieved with a large TPC. This measurement, independently of the detector resolution, is limited to the momentum region where kaons are separated from other particles, mostly pions. This limitation is particularly important in the fixed target experiments where the total momentum is dominated by the longitudinal momentum originating from the boost. In the CERES setup the average momentum to transverse momentum ratio is $p/p_T \sim 5$.

The measurement of charged kaons using the kink decay topology, $K^+ \to \mu^+ + \nu$, needs a large detector in the homogeneous magnetic field to measure the momentum of both charged kaon and muon. A large detector is also needed to increase the probability of a decay in the TPC.

The K^+_τ decay into tree pions took its name from the topology observed in the bubble chamber in the homogeneous magnetic field. The three outgoing particles create a τ shape a unique signature for the K^+_τ. The observation of two particles, τ and θ, with the same mass and lifetime but with different parities lead to the question of violation of parity in weak decays [27]. In a non-uniform field, reconstruction of the tree tracks meeting at one point is more complicated.

Decay of the K^0_S into two pions seems the most promising detection method for the CERES setup. The strange mesons can be identified as a peak in the invariant mass spectrum of the decay products. The large combinatorial background can be compensated either by the large amount of data available for statistical analysis or topological cuts on the reconstructed secondary vertex.

In this feasibility study the hadronic decays of neutral and charged kaons will be discussed. Two scenarios of the reconstruction setup will be described and compared.

3.2 Reconstruction scenarios

The feasibility of four scenarios for the reconstruction of strange mesons were studied, two for charged and two for neutral kaons:

- $K^0_S \rightarrow \pi^+\pi^-$, where both pions are detected by the TPC. Since the TPC is located 3.8 m downstream all K^0_S will decay before the TPC. The fiducial volume, set arbitrarily to $\lambda_z < 100$ cm, was chosen due to deterioration of the TPC momentum resolution for the non-primary particles. The disadvantage of this topology is poor secondary vertex reconstruction capabilities of the TPC alone.

- $K^0_S \rightarrow \pi^+\pi^-$, where pions are detected by the TPC and silicon detectors. The advantage of this topology is a very good vertex reconstruction capability of the silicon detectors. This topology has limited fiducial volume due to the condition $\lambda_z < 4$ cm and thus the acceptance is smaller than in the scenario with the TPC alone. Since decay position depends on the momentum $\lambda = \beta\gamma c\tau$, this topology will suppress the high momentum tracks.

- $K^+ \rightarrow \pi^+\pi^+\pi^-$called K^+_τ, with decay point before the TPC. When this topology is observed inside a large bubble chamber in a homogeneous field it has the shape of a letter τ and three secondary tracks meeting at one point give a clear signal of a K^+_τ. This advantages can not be used in the CERES setup in a straightforward way due to the relatively small TPC and mostly due to the inhomogeneous field. This topology can nevertheless be used with the decay point before the TPC and three pions reconstructed in the TPC. The main disadvantage of this topology is relatively low branching ratio $r = 5.6\,\%$ and relatively long decay length of K^+, $c\tau = 3$ m. The upper limit on the longitudinal coordinate of the decay length has to be lower than the position of the TPC, while on the other hand momentum resolution deteriorates for non-vertex tracks. For this study the fiducial volume in the longitudinal coordinate was set to $\lambda_z < 100$ cm. Probably a longer fiducial volume can be used.

- The K^+_τ topology with decay before the SD. This topology has a very small cross-section due to the low branching ratio and significantly reduced fiducial volume $\lambda_z < 4$ cm. This topology is similar to that of D^+ decay. If this topology can be

observed, with the help of the vertexing possibilities of the silicon detectors it can be used for the tuning of the cuts for D^+ reconstruction.

3.3 Acceptance simulation program

The program to study the acceptance and kinematic properties of decay products was developed in the Root environment [28]. The standard classes were used for random number generation, relativistic transformations, 2– and 3–body decay simulation and finally for data storage and visualization. The program does not include simulation of the propagation of the particles in the magnetic field, multiple scattering, detector fine-structure or response. The procedure was kept simple to estimate gross properties of the different topologies.

The simulation procedure is the following:

- Momentum vectors of a number of primary K^0_S or K^+_τ are generated according to the thermal distribution. Transverse momentum follows m_T exponential distribution:

$$\frac{dN}{dp_T} = p_T \exp\left(-\frac{\sqrt{m^2 + p_T^2}}{T}\right) \tag{3.1}$$

  where m is the kaon mass, p_T is the transverse momentum, and T is the inverse slope parameter, set to $T = 220$ MeV. Rapidity follows Gaussian distribution with width $\sigma = 1.1$ and azimuthal distribution is flat. For more efficient study of the detector acceptance a flat distribution of transverse momentum, rapidity and azimuth can be used. Additionally different inverse slope parameters were used, to estimate properties of decay in relation to particle momentum composition. Since this simulation is for qualitative study, the parameters of the simulation are not exact values expected from the systematics of strange particles production.

- Particles are boosted by the rapidity $y = 2.913$ for the 160 GeV/c case and $y = 2.265$ for the 40 GeV/c scenario.

- 2–body decay for K^0_S and 3–body decay for K^+_τ is simulated. Decay is realized by the standard class *TPhaseSpaceGen*.

- Primary particle: K^0_S or K^+_τ are accepted if two criteria are fulfilled:

  - polar angle of all secondary pions is in the acceptance $8^0 < \theta_{lab} < 15^0$

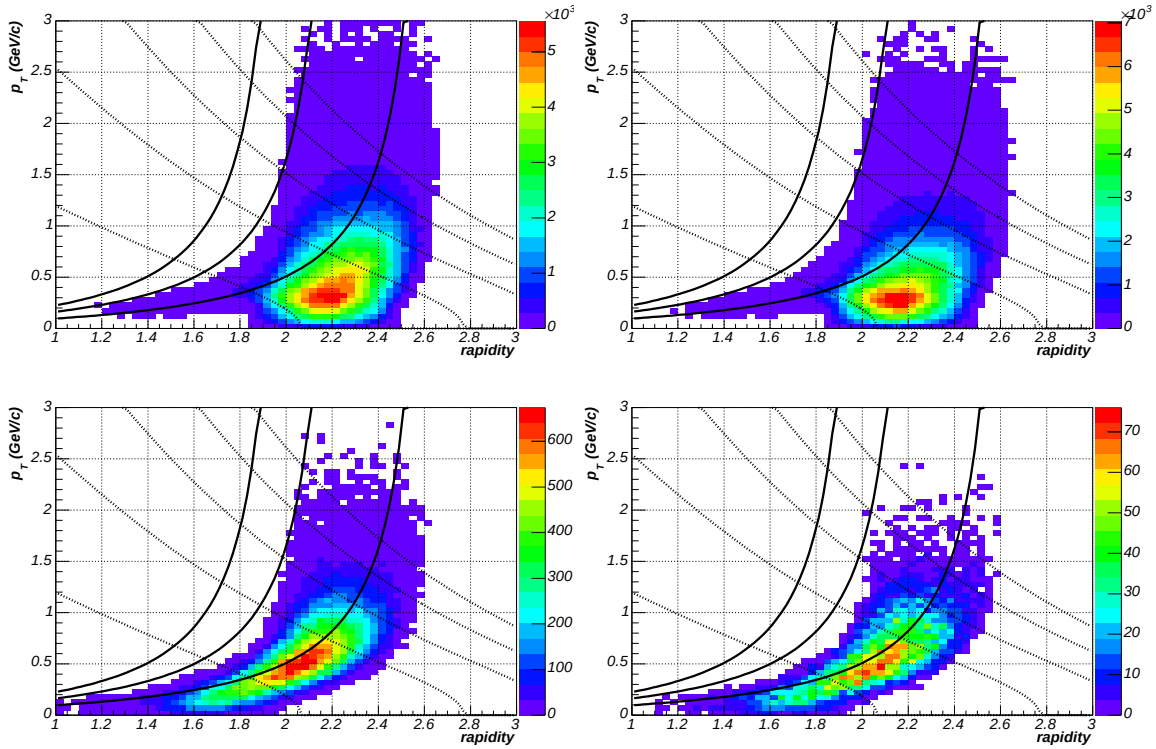

Figure 3.1: Acceptance in the transverse momentum – rapidity space. Upper row: K_S^0 decaying before the TPC (left) and the SD (right). Lower row: K_τ^+ decaying before the TPC (left) and the SD (right)

  - decay point is in the fiducial volume of $\lambda < 100$ cm for the TPC and $\lambda < 4$ cm for the setup TPC–SD

- Both primary particles and decay products are stored in a Root tree as *TParticle* objects

Additionally, for 2–body decay additional cut on opening angle $\psi > 0.01$ rad, corresponding to double track resolution of the CERES TPC can be applied.

3.4 Acceptance for different scenarios

The acceptance in the transverse momentum – rapidity plane for the four scenarios is shown in Fig. 3.1, where the solid lines represent constant polar angle of the kaon of 8^0(higher rapidity), $12^0$and 15^0. Dashed lines represent constant momentum of the kaon of 2, 4, 6, 8 and 10 GeV/c. For both cases: K_S^0 and K_τ^+ the primary track is pointing

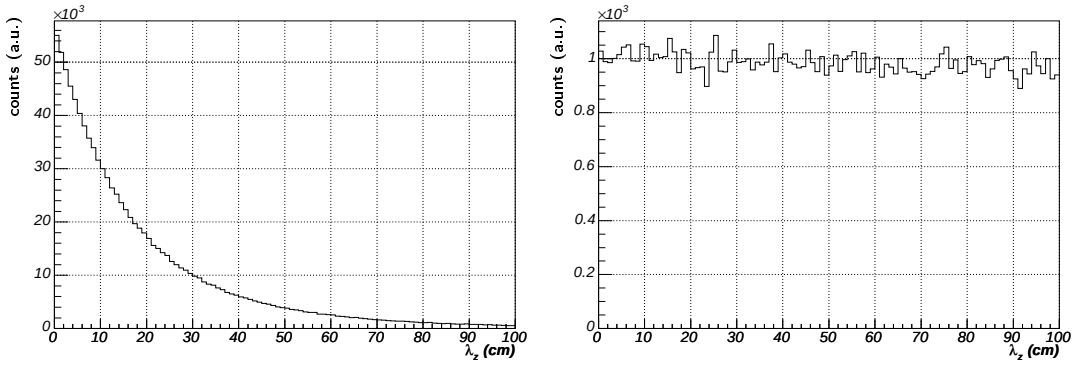

Figure 3.2: Longitudinal coordinate of the decay vertex for K_S^0(left) and K_τ^+(right)

into the inner part of the TPC – for K_S^0 the polar angle is less than $\theta < 10^0$ and for K_τ^+ it is around 8^0. The structure of the signal for K_S^0 looks more promising for the studies of the strange meson production, since it is concentrated in a box shape with rapidity $2 < y < 2.6$ and transverse momentum $p_T < 2.5$ GeV/c. The signal for K_τ^+ have a banana type structure along polar angle $\theta \simeq 8^0$; the rapidity spans one unit from $y = 1.5$ to $y = 2.5$ but the transverse momentum is nowhere fully represented.

The distribution of the longitudinal coordinate of the decay vertex for K_S^0 and K_τ^+ is shown in Fig. 3.2. Most of the K_S^0 decays in the first 50 cm while distribution of K_τ^+ decay length is practically flat in the fiducial volume from vertex up to the TPC. The structure of the decay length is a convolution of the particle intrinsic decay length and $\beta\gamma$ factor.

The distribution of the $\beta\gamma$ for the four scenarios is shown in Fig. 3.3. For K_S^0 $\beta\gamma$ peaks at around 5 and then drops to zero. The distribution is different for the setup with the TPC and the TPC-SD. The suppression of high $\beta\gamma$ tracks, due to limited fiducial volume is clearly visible. For K_τ^+ the distribution of $\beta\gamma$ does not differ between the two scenarios, and the distribution is a broad peak from 3 to 10.

The overall acceptance for the scenarios presented varies by three orders of magnitude. The highest acceptance $\eta = 4.3\%$ have the K_S^0 topology without SD detectors. With the requirement of the decay before SD the acceptance drops by a factor of 5 to $\eta = 0.79\%$. The acceptance of the K_τ^+ with decay before the TPC is as low as $\eta = 1.4 * 10^{-3}$ and with the requirement of a decay before the silicon detectors the acceptance drops 25-fold to $\eta = 6.1 * 10^{-5}$. The values presented are collected in the Table 3.1. The numbers presented above vary slightly when modifying the inverse slope parameter. In general, higher transverse momentum tracks have greater acceptance in the K_S^0 decays with the TPC alone and lower acceptance in the remaining scenarios.

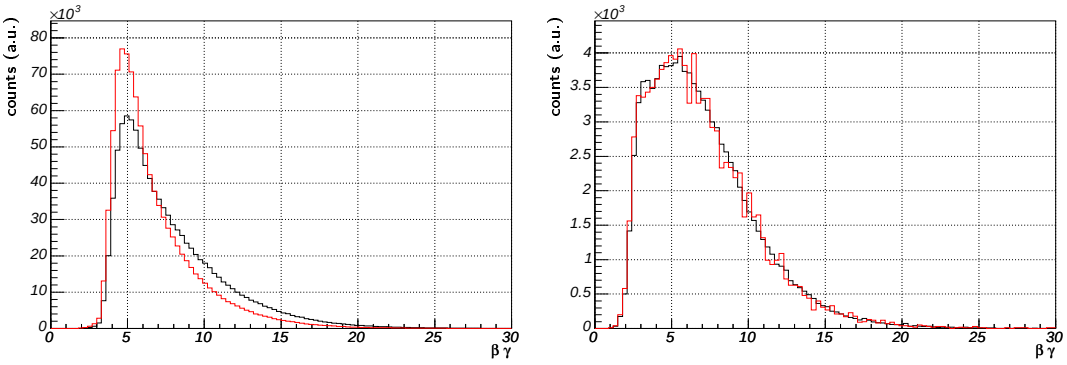

Figure 3.3: Distribution of $\beta\gamma$ for K^0_S(left) and K^+_τ (right). The red line is for the setup with the TPC only and the black for the setup with the TPC+SD. Histograms are scaled to fit in the integral.

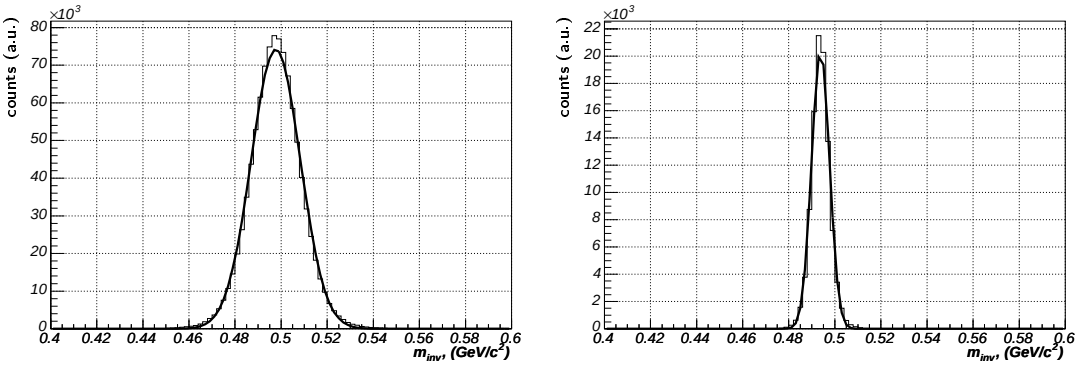

Figure 3.4: Estimation on the invariant mass resolution for K^0_S (left) and K^+_τ (right).

The simulation procedure can be upgraded with the simple model of invariant mass resolution. The momentum of each track is smeared according to the Gaussian distribution with the width:

$$\Delta p/p = 0.02 + 0.01p \tag{3.2}$$

and the spread of the angles smear is $\Delta\phi = 3\,\mu$rad and $\Delta\theta = 3\,\mu$rad. With this simple smearing, the resolution of the invariant mass can be estimated. This estimation does not represent the detailed structure of the detector and multiple scattering but can be used to estimate the order of magnitude of the the invariant mass resolution. The distributions are shown in Fig. 3.4. The resolution is 10 MeV/c^2 for K^0_S and 4 MeV/c^2 for K^+_τ. It can nevertheless be expected that the true resolution will be worse than the simulated one.

	K^0_S TPC	K^0_S TPC-SD	K^+_τ TPC	K^+_τ TPC-SD
acceptance (η)	$4.265 * 10^{-2}$	$7.95 * 10^{-3}$	$1.462 * 10^{-3}$	$6.16 * 10^{-5}$
branching ratio (r_B)	68.61 ± 0.28 %	68.61 ± 0.28 %	5.59 ± 0.05 %	5.59 ± 0.05 %
overall signal	$5.8 * 10^7$	$1.1 * 10^7$	$1.6 * 10^5$	$6.9 * 10^3$
background	$7.5 * 10^{10}$		$9 * 10^{11}$	
noise	$2.7 * 10^5$		$9.5 * 10^5$	
overall significance	215		0.17	

Table 3.1: Numerical values for the signal, background and significance.

3.5 Estimation of the significance

It can be estimated if a given topology can be observed with the available statistics without any kinematic or geometrical cuts. In the case where the topology can not be observed without cuts it can be calculated how strong suppression of the background is necessary to observe the signal. For this study an estimation of the background is necessary, in addition to estimating the signal

The expected signal S can be calculated according to the formula:

$$S = N n g_\sigma r_B \eta \tag{3.3}$$

where: N is the number of available events, n is the expected multiplicity of the investigated particle, g_σ is the fraction of the signal in the peak in the invariant mass spectrum, r_B is the branching ratio and η is the acceptance for a given topology.

For the first approximation the number of expected kaons of every type can be set at 100 per event. The number of events collected by the CERES experiment is $3 * 10^7$, the area of the accepted signal was set to $\pm\sigma$ and thus $g_\sigma = 0.68$. The numerical values for the branching ratios and acceptance as well as the final value of the expected signal are presented in Table 3.1.

Also the background can be estimated with the simulation study. It is important to note that the background estimated by the presented simulation can be used only for studies of the scenario feasibility. It can not be used to subtract combinatorial background from the invariant mass spectra reconstructed obtained with real data. The later application will need very precise estimation of the background and will be discussed in the next chapter.

The simulations procedure is the following:

- The number of primary positive pions is generated with the transverse momentum following Boltzmann distribution with the inverse slope parameter $T = 170$ MeV,

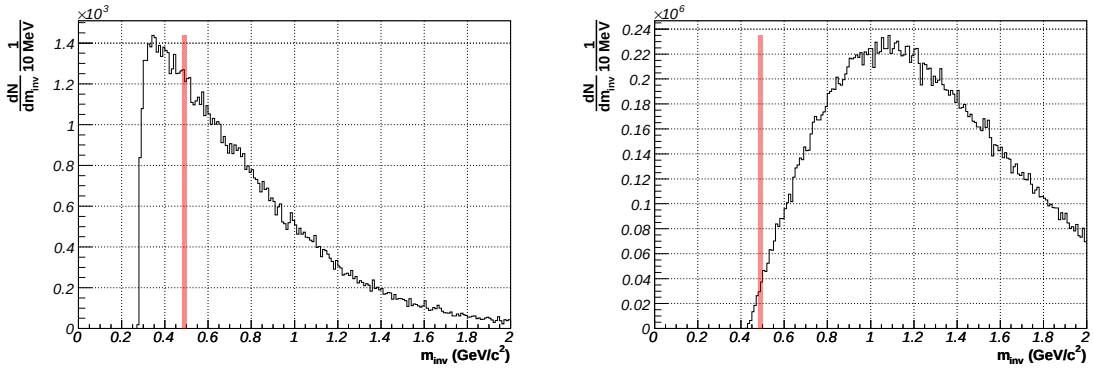

Figure 3.5: Combinatorial background for 2–body K^0_S decay (left) and 3–body K^+_τ decay (right). A red box represents the position of the kaon peak.

rapidity following Gaussian distribution with width $\sigma = 1.1$ and flat in the azimuth. The cut on the polar angle of $8^0 < \theta < 15^0$ is applied. The same procedure is repeated for negative particles. The number of both positive and negative pions in the acceptance equals 300 and corresponds to the number of tracks in the CERES TPC.

- The invariant mass spectrum is calculated for all pairs for the K^0_S case and all triples for the K^+_τ case to simulate the combinatorial background. The resulting spectrum is stored in a histogram.

- The most important limitation of this estimation of the background is the lack of dependence on geometrical cuts. Those issues can only be properly addressed with the full Monte-Carlo simulation. The spectrum does not contain any additional cuts, in particular the cut on the relative azimuthal angle in case of the K^+_τ study will change the shape of the spectrum at masses above the kaon mass.

The resulting invariant mass distributions shown in Fig. 3.5 represent the combinatorial background for one event. For the K^0_S, the signal sits behind the maximum of the combinatorial background, for K^+_τ the signal sits at the rise of the background. The rise of the background is very steep for K^0_S and moderate for K^+_τ. For K^0_S the number of background entries, in the same range as for the signal, is at $2.5 * 10^3$ and for K^+_τ it is at $3 * 10^4$. The number of background entries for the whole data set is shown in Table 3.1.

The expected significance Σ can be estimated with the approximate formula:

$$\Sigma = S/\sigma(B) = S/\sqrt{B} = \frac{N n r_B \eta}{\sqrt{Nb}} = \frac{1}{\sqrt{N}} \frac{n r_B \eta}{b} \tag{3.4}$$

where: S is the total signal as calculated above, B is the total background and $\sigma(B)$ is the fluctuation of the background. Since the background follows Poisson distribution the fluctuations of the background equal $\sigma(B) = \sqrt{B}$ where b is the background per event and N is the number of events.

The results of the calculations for the setup with the TPC only is shown in the last row of Table 3.1. In the case of K^0_S the overall significance is around 200 and in the case of K^+_τ the significance without topological cuts is 0.17 – an order of magnitude less than statistical fluctuations.

From the estimation of the signal and the background the number of events necessary to observe a significant peak $S = 3N = \sqrt{9B}$ can be calculated. The formula reads:

$$N = \frac{9b}{(ng_\sigma r_b \eta)^2}$$

where $N = 9 * 2.5 * 10^3/(10^2 * 0.7 * 0.68 * 4.2 * 10^{-2})^2 = 1 * 10^4$ events. With this number of events a peak in the invariant mass should be detectable.

3.6 Summary

This short simulation shows that it is possible to reconstruct the spectrum of the K^0_S with the TPC alone without topological cuts. The acceptance has a box shape which will help in the fitting of the transverse momentum spectrum.

This scenario would allow the study of the neutral strange meson production in the rapidity region spanning 0.6 units, in the range $2.0 < y < 2.6$. The limit on the transverse momentum can not be addressed in this simulation. On one hand, the acceptance grows with transverse momentum, on the other hand the momentum resolution drops and the peak becomes wider and thus the extraction is more difficult.

From the point of view of the analysis presented in this chapter one can not fully compare the scenario with and without SD. Both methods have different experimental difficulties – for the scenario without the cuts, the main difficulty is the large background and for the scenario with SD and topological cuts the main difficulty is estimation of the efficiency. Both measurements are complementary and will give additional insight into the systematical error.

The identification of the K^+_τ will need extremely strong topological cuts to suppress the background. The full reconstruction of the K^+_τ spectrum will have to solve two issues – precise simulation of the strong topological cuts and the fit of the transverse momentum

spectrum to obtain a total yield. Another possibility is to reconstruct only the ratio of the K^+/K^- and combine the ratio with the mean value of $0.5 * (K^+ + K^-)$ which is equal to K^0_S.

4 Reconstruction of the K^0_S in the CERES data

The reconstruction of the physical quantity from the experimental data is a multi step procedure. The first steps, common to every analysis of CERES data were described in the previous chapter.

The K^0_S reconstruction procedure is decomposed into two parts. The first part, data processing, is responsible to create histograms of the signal and the background for every transverse momentum – rapidity bin as well as a number of histograms for quality assurance. This chapter will focus on the issues of data processing, in particular on the proper estimation of the background. The input for data processing are tracks, the output are histograms of the invariant mass spectrum.

Second part of the reconstruction, the final analysis, deals with the extractions of the K^0_S peak and combining the raw yield from data with the efficiency obtained from Monte-Carlo studies. This procedure will be described in Chapter 6 after description of the Monte-Carlo simulation in Chapter 5. The output of this analysis are the transverse momentum and rapidity spectra of the K^0_S, quantities that could be directly interpreted.

4.1 Strategy

The main device of CERES in the run 2000 is the radial drift TPC. The tracks from the TPC can be combined into pairs and the invariant mass will give a signal of K^0_S. The additional information of the topology of the tracks coming from K^0_S can be used.

One option is to reconstruct a position of the secondary vertex using TPC tracks. The tracks reconstructed by the TPC are in a cone, thus the reconstruction of the crossing point is difficult. The resolution of the secondary vertex reconstruction with the TPC alone, in longitudinal direction, is around 6 cm [29]. The distribution is not Gaussian and have long tails, thus the cut is not very effective in removing the background.

The precision but also the level of complication of the reconstruction can be increased using the information from the silicon detectors. One option, as discussed in the feasibility studies, is to make full reconstruction of the kaons decaying before silicon detectors. This

possibility was explored in details in another project described in Ref. [30]. The main disadvantage of this approach is heavy dependence on the results from the Monte-Carlo studies.

For neutral kaons decaying after the silicon detectors the absence of the SD hit can be used as an additional information. Anti-matching cut can significantly reduce the background, at a price of undetermined reconstruction efficiency.

Finally, the simplest option was chosen, to not use any topological information. In short, the disadvantage of the CERES setup – low vertexing capabilities – is at the same time its important advantage – the efficiency of the track reconstruction does not depend strongly on the origin of the track. This features relaxes the dependency on the efficiency estimation using Monte-Carlo simulations.

4.2 Reconstruction chain

The programs to process data were developed in the Root environment. They are composed out of a few classes for the actual processing and macros for graphical presentation. The processing was performed using the batch farm at GSI controlled by the LSF batch jobs system. The job submission is data-driven, for every unit one job is submitted.

The processing program starts with loading a chunk of data into the memory. The internal representation of the tracks is in the polar coordinate space (p, θ, ϕ). This representation is the closest to the actually measured.

In case of the K^0_S analysis all particles are assumed to be pions. In principle some selection can be made to suppress protons and charged kaons; however, this procedure would not improve the signal much but would bring another source of systematic error.

To have a choice of events for the event mixing, it is convenient to have as many events at once in a memory as allowed by the computing resources. For that sake an efficient representation was developed. The tracks were stored in plain tables using single-precision floating-point numbers. This representation allowed loading 20 consecutive bursts, which gives around 6000 events.

4.2.1 Momentum

In the CERES setup two estimations of the momentum are used, based on two or three-parameter fit. These momenta are referred as *pcor2* and *pcor3* respectively. Two-parameter fit takes into account the vertex as one of the points. For high momentum, rigid tracks,

when the displacement in the magnetic field is small, the additional distant point at vertex improves the momentum resolution. This is not the case for the low momentum tracks. The resolution of low momentum tracks is limited by the multiple scattering and distant points do not improve it.

Since the expected precision as a function of the momentum is known, one can create combined momentum (*pcomb*) taking weighted average of the two and taking into account the expected resolution:

$$p_{comb} = \frac{p_2/\sigma_2^2 + p_3/\sigma_3^2}{1/\sigma_2^2 + 1/\sigma_3^2} \tag{4.1}$$

where p_2 and p_3 are the momenta from the two and three-parameter fits respectively and the resolutions σ_2 and σ_3 are calculated:

$$\sigma_2^2 = \sigma_{20}^2 + (\sigma_{21} * p_2)^2 \tag{4.2}$$

Using the parameters: σ_{20}, σ_{21}, σ_{30} and σ_{31} obtained by the simulation studies.

For most types of the analyses using combined momentum provide the best resolution, but the situation changes while discussing secondaries. Using combined momentum could improve the resolution for high momentum neutral kaons, but the high momentum means also high $\beta\gamma$ and decay far from the vertex. The peak resolution as a function of the momentum and rapidity of the primary kaon for both reconstruction strategies using *pcomb* and *pcor3* is studied in details in Chapter 5. During the processing stage both momentum options were used; however, in the final results, presented in Chapter 6, the three-parameter fit was employed.

4.2.2 Azimuthal and polar angle

In the CERES setup two methods of the reconstruction of the angles are used. The main method was optimized for the primary tracks. The second method which is actually used for K_S^0 analysis was initially used as an intermediate step of the tracking; only recently with the production step3c v2 the local angles were stored on tape.

During the travel of the tracks from fireball to the detector without magnetic field, the polar and azimuthal angles of position and momentum are the same. During reconstruction, the tracks found in the TPC where propagated to the most probable place of the scattering – the mirror of the second RICH detector (*R2M*). The polar coordinates of the intersection of the propagation with the mirror are used as the polar coordinates of the momentum. This procedure improves the resolution at a price of forcing the origin of the

tracks to the primary vertex. In this analysis these angles are used for the cuts on the fiducial volume of the track, but are not the optimal choice for the reconstruction of the neutral kaon peak.

For actual reconstruction the local angles are used. The angles are recalculated from the four original parameters of the fit X_0, X_1, Y_0 and Y_1, that represent the offset and the slope of a straight line. From these parameters the local angles θ_L and ϕ_L are calculated:

$$\theta_L = \arctan\left(\frac{x * X_1 + y * Y_1}{r}\right) \tag{4.3}$$

$$\phi_L = \arctan\left(X_1/Y_1\right) \tag{4.4}$$

where $r = \sqrt{x^2 + y^2}$ and the coordinates x and y are calculated at a given plane z:

$$x = X_0 + z * X_1. \tag{4.5}$$

Summarizing, the best estimation of the angles for the analysis of the primary tracks is provided by the *R2M* angles and for the secondaries by the local angles. For internal tracking usage and for study of the double track resolution additional angle is provided – the ϕ angle of the first hit in the TPC.

4.3 Data selection

The data sample for the analysis was prepared with a set of cuts. Four types of the cuts were used: event cuts, events association cuts, track cuts and finally pair cuts. Also fifth type of the cuts was tried – a cut on a single track, belonging to a given pair. This cut was initially intended for the removal of the tracks from the conversions, but in the final data reported here the cut was not used.

4.4 Event cuts

Event cuts are designed to prepare a clean sample of data within a given centrality class. The event cuts are applied before tracks are loaded, using the variables filled during data production.

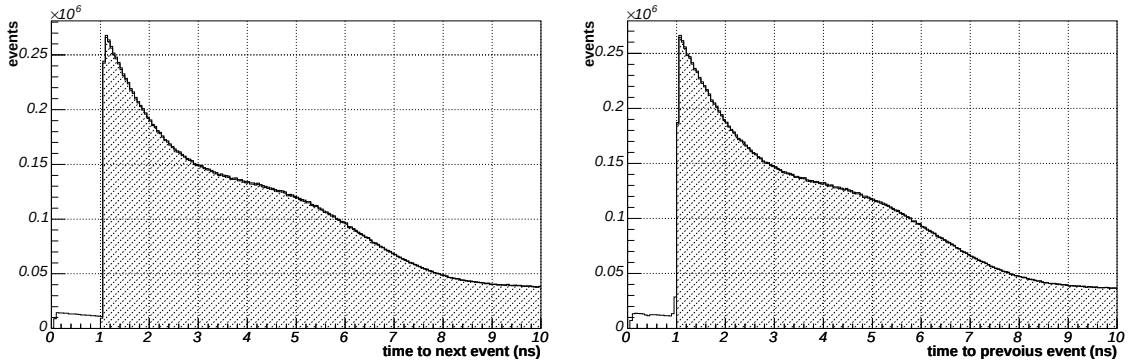

Figure 4.1: Before-after protection. Time to the previous (left) and to the next event (right)

bit number	description	number
0	beam	292 562
1	minimum bias	462 089
2	central events	31 022 653
8	random pulser	141 618
12	TPC laser	11 925

Table 4.1: Trigger codes and the number of triggers

4.4.1 Beam and trigger

The first event cut is on the signal from the beam counters BC1 and BC2. The distributions of the BC1 and BC2 were calibrated during step0 production to be centered at 0 and have the width equal $\sigma = 1$. The cut was placed at $B \in (-3, 3)$.

To prevent overlapping events in the TPC a cut on the time to proceeding and following beams is applied: $\Delta t > 1000\,\mu$s. The Fig. 4.1 shows the distribution of the time to previous (left) and next (right) event. This cut was applied on-line during most of the data taking period, thus the cut removes only small fraction of the data sample.

After the cut on the conditions of the event, the trigger cut was applied. Codes for trigger and the number of events are presented in Table 4.1. Only central events with code 2 were selected.

4.4.2 Impact parameter and the centrality

The geometry of two approaching nuclei along the beam axis are depicted in Fig. 4.2. The event is characterized by the impact parameter b. The impact parameter, together with the type of the nuclei and the beam energy defines the conditions of the collision.

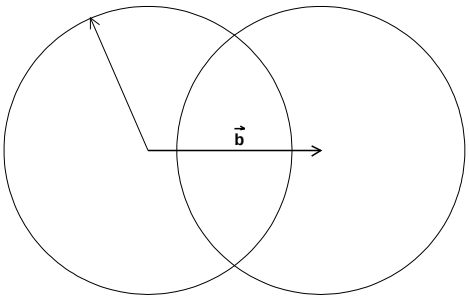

Figure 4.2: Geometry of two approaching nuclei in the transverse plane

Experimentally, the impact parameter is not measurable directly; instead, two methods are used to measure the centrality of the collision. The first method is a direct measurement of the spectators using Zero Degree Calorimeter (ZDC). With the number of spectators measured, one can calculate the number of participants and using some model of the collision calculate the impact parameter. It is interesting to note, all four RHIC experiments have the same type of ZDC detectors which help comparing the centrality in the model independent way [31].

Another possibility is based on the assumption, the energy dissipated during the collision, reflected in the total multiplicity, is a measure of the centrality. The centrality is measured as a fraction of the geometrical cross-section (σ_G), defined as the quantiles of the multiplicity distribution of the minimum bias events:

$$f_\sigma(M) = \int_M^{Mmax} dm \, \frac{n(m)}{N} \tag{4.6}$$

where $f_\sigma(M)$ is the fraction of the geometrical cross-section for a given cut on the minimum multiplicity M, $n(m)$ is the number of events with the multiplicity m in the min–bias sample and N is the total number of events in the min–bias sample. Actually the fraction of σ_G are not exactly quantiles, because the centrality is inversely correlated with the multiplicity. The fraction of the geometrical cross-section $f_\sigma = q$ corresponds to quantile $1 - q$.

To determine the centrality, one does not need an absolute measurement of the multiplicity, a relative measurement is sufficient. Since the number of tracks is a subject of statistical fluctuations, it is also important to cover a large part of created tracks.

This method of the centrality measurement is used by the CERES experiment. Total multiplicity can be measured in the tracking detectors: the TPC and SD as well as in the hadronic calorimeter Multiplicity Counter (MC) measuring the total multiplicity. The

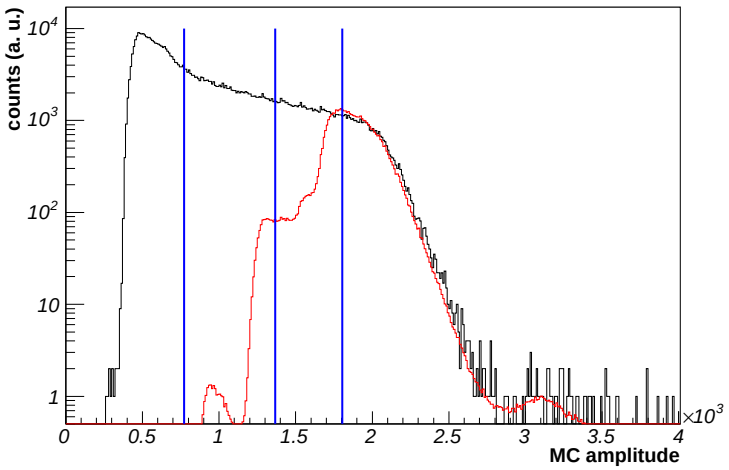

Figure 4.3: Signal from Multiplicity Counter. Black histogram: minimum bias data, red histogram: uncalibrated central data (arbitrary scaling), blue lines show multiplicity cuts corresponding to centrality of 50%, 20% and 7% of the geometrical cross section.

distribution of the signal from the MC counter, proportional to the multiplicity, is shown in Fig. 4.3. The black histogram shows minimum bias data, the red histogram shows the central data before calibration, scaled to match the minimum bias data at the slope. The central events sample is composed of two subsamples with the centrality of 7% and 20%.

The two distributions: min–bias and central shall have the same shape of the right part. This is not the case, for the raw signal, due to the fluctuations of the gain of the Multiplicity Counter. The data are calibrated on the unit by unit basis. The high multiplicity tail is described by the function

$$n(m) = \frac{A}{1 + \exp\left(\frac{m-B}{C}\right)} \tag{4.7}$$

where $n(m)$ is the multiplicity distribution to be fit and A, B and C are the fit parameters. The amplitude of the MC is scaled by a factor B/B_{ref}, where the B_{ref} is the result of the fit for the reference low intensity min–bias sample. After the calibration, to every event centrality can be assigned using relation in Eq. 4.6. The calibration of the amplitude of the MC detector and the calculation of the centrality of the event is a standard procedure in the reconstruction chain and further details of the procedure are presented in [32].

The distribution of the calibrated centrality is shown in Fig. 4.4. The sample is composed of three regions. The first is the central sample of 7% followed by the sample with centrality of 20%. These are followed by a tail extending up to 30% and some empty events. The

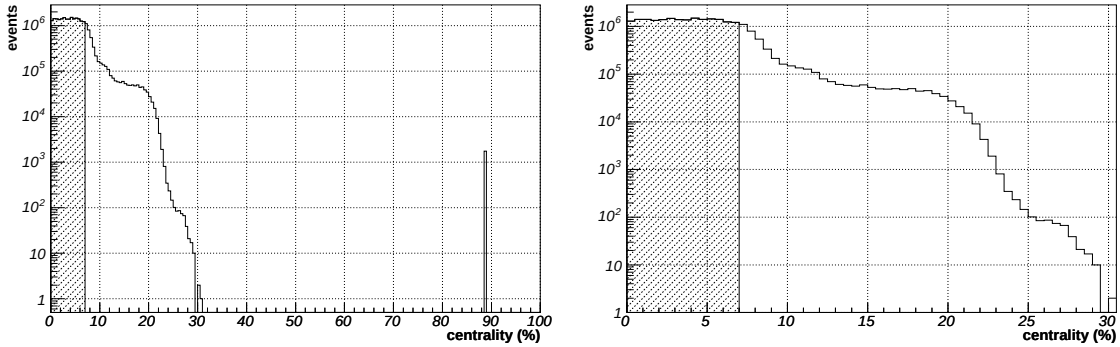

Figure 4.4: Calibrated centrality of the collected events, left panel shows the full spectra while the right is zoom on central events.

right panel zooms on the central events. The shaded region shows the data used in further analysis.

After the centrality of the sample is determined the mean impact parameter and the number of participants can be calculated using for example Glauber model. The Glauber model will be discussed when the results will be compared to other experiments in Chapter 7.

4.4.3 Multiplicity in the TPC

The cuts discussed above shall select a sample of clean central events. This is not the case as illustrated in Fig. 4.5 showing the distribution of the multiplicity in the TPC.

The number of tracks presented here was calculated during the step3c production with the selection on the polar angle $0.12 < \theta < 0.24$ rad and the number of hits $nHits \geq 10$. On the left side of the peak practically empty events are visible, on the right side a shoulder develops, probably due to overlapping events. To remove potentially pathological events a cut is placed at $3\,\sigma$ around the center at $150 - 320$ tracks which removes around 1% of the events.

4.4.4 Efficiency of the event cuts

The effect of the consecutive event cuts is presented in Fig. 4.6 for the data sample in the production prod012 and in Fig 4.7 for prod013. The left diagram shows the total number of events after a given cut was applied. The right panel shows percentage of the events rejected by a given cut. Summarizing, after all cuts around $21 * 10^6$ events are used for the analysis and around $9 * 10^6$ events are rejected, which corresponds to the quarter of

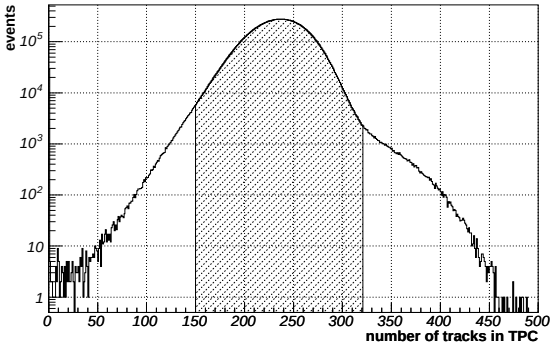

Figure 4.5: Multiplicity in the TPC.

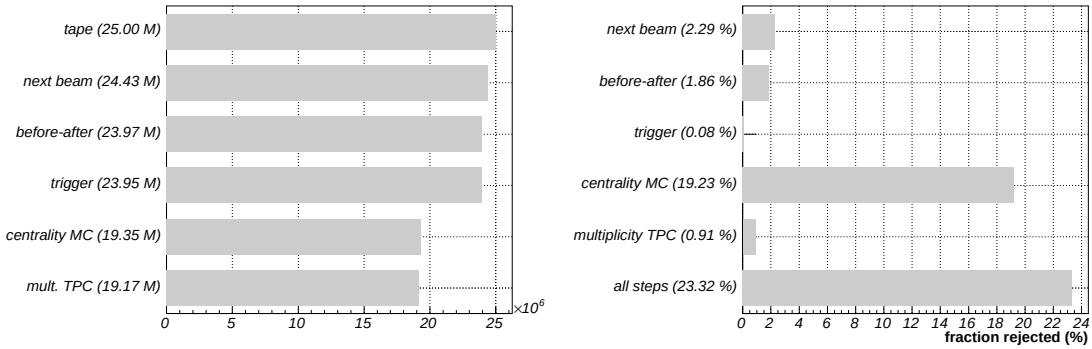

Figure 4.6: Number of events after consecutive cuts for data sample in the production prod012

the total statistics. The most important is the cut on the centrality measurements from MC detector removing around 25% of the statistics.

There is always risk, the cleaning of the sample will bias it. In this case the most important cut is the centrality selection. The removal of pathological events changes the sample by 4%. Even if the pathology is correlated with the centrality distributions, these cuts shall not significantly bias the sample.

4.5 Track cuts

4.5.1 Polar angle and the number of hits

The number of fitted hits as a function of the polar angle is shown in Fig. 4.8. In the range $\theta \in (0.13, 0.22)$ rad the tracks cross the whole active area and the number of fitted hits peaks at 18 hits. In the range $\theta < 0.13$ rad the number of hits rapidly falls. In the

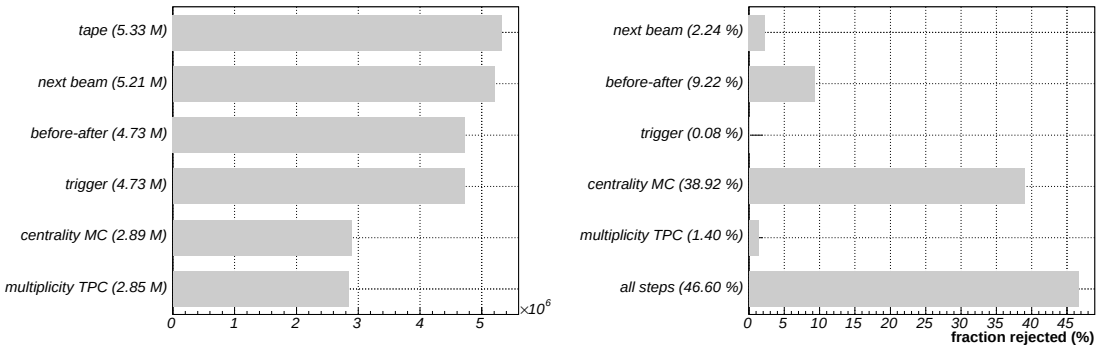

Figure 4.7: Number of events after consecutive cuts for data sample in the production prod013

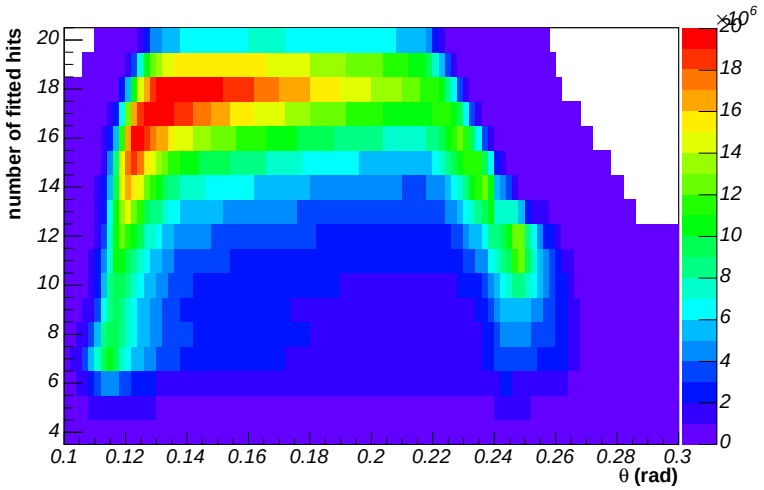

Figure 4.8: Distribution of the number of fitted hits as a function of the polar angle

range $\theta \in (0.22, 0.28)$ rad the number of hits falls slowly with θ. On the basis of the presented distribution the cut can be applied on theta around $\theta \in (0.12, 0.28)$ and a cut on the number of hits depending on θ like:

$$\begin{aligned} N_{hits} &\geq 10 & \theta &\in (0.12, 0.22) \\ N_{hits} &\geq 10 - (\vartheta - 0.22) * 150 & \theta &\in (0.22, 0.28) \end{aligned} \tag{4.8}$$

There is a strong correlation between the polar angle and the maximum possible number of hits; thus, the cut on the number of hits independent on the polar angle is an implicit cut on the polar angle in the range $\theta > 0.22$ rad. The distribution of the number of hits is shown in Fig. 4.9, for positive and negative tracks. The shaded area represents selected region.

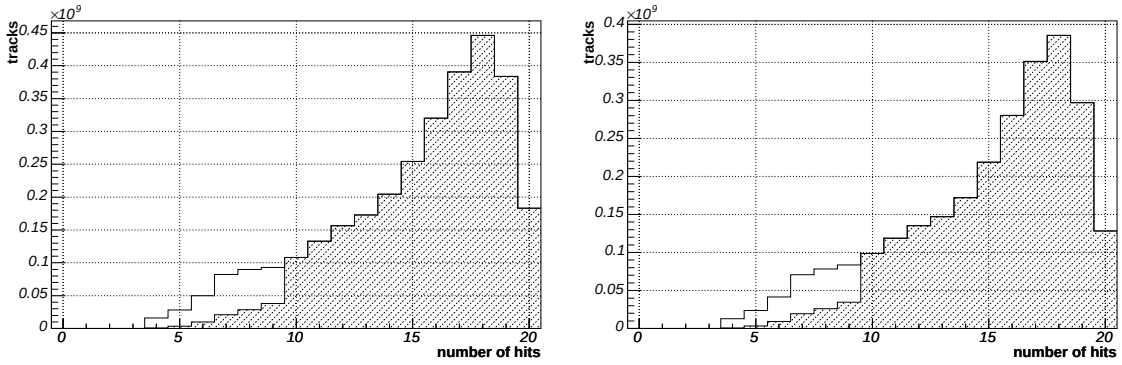

Figure 4.9: Distribution of the number of hits for positive (left) and negative (right) tracks. Shaded area shows the selected region

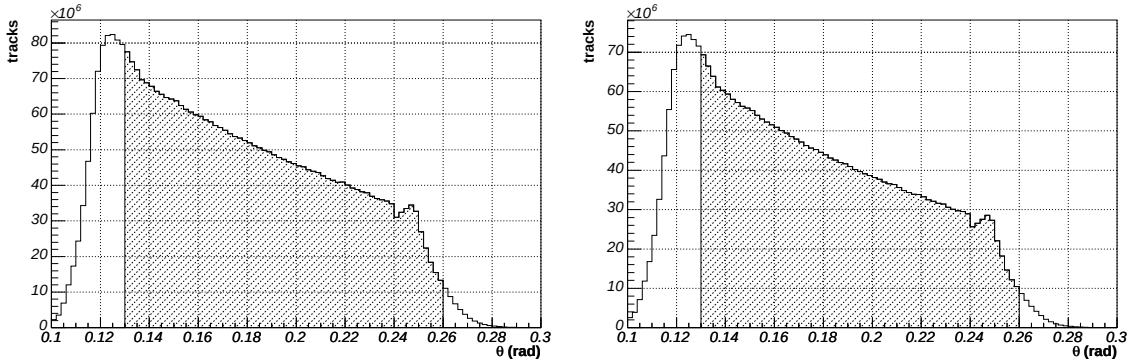

Figure 4.10: Distribution of the polar angle for positive (left) and negative (right) tracks. Shaded area shows the selected region

The distribution of the tracks in the polar angle is shown in Fig. 4.10. The left panel shows the positive and the right panel the negative charge. The distribution is peaked at $\theta \simeq 0.13$ rad. and falls rapidly toward low angles and slowly to high angles up to $\theta \simeq 0.24$ rad. then a shoulder is visible. This shape is dominated by the geometry of the TPC. The selection of the polar angle has significant impact on the signal in some rapidity ranges. Making too conservative cut will remove significant part of the signal, on the other hand too generous acceptance can lead to problems is reproducing the efficiency in the Monte-Carlo studies. A reasonable choice to place the cut, justified by the simulation studies, is $\theta \in (0.13, 0.26)$ rad.

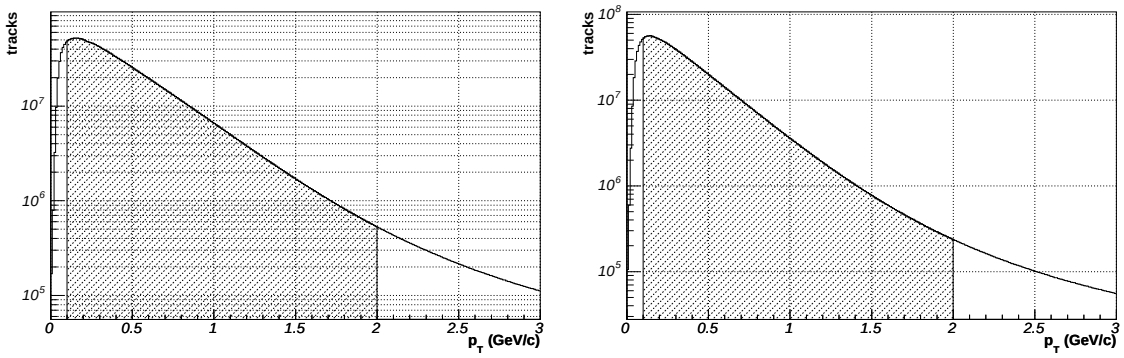

Figure 4.11: Distribution of the transverse momentum for positive (left) and negative (right) tracks. Shaded area shows the selected region

4.5.2 Transverse momentum

In the CERES setup the tracking efficiency deteriorates at low momentum and at high momentum the resolution suffer. The minimum possible momentum cut is placed at $p_T > 100$ MeV/c and the safe cut, used for most of the analyses is set at $p_T > 150$ MeV/c.

It is difficult to use the safe cut in the reconstruction of the K^0_S. For low momentum kaons the decay topology is the following: the primary kaon moves along the beam line and decays into two pions back-to-back. The decay momentum of the K^0_S is $q = 209$ MeV/c and this is practically the only source of the transverse momentum, thus each pion takes around $p \simeq 200$ MeV/c and depending on the orientation a part of this momentum goes into transverse plane. With the cut of $p_T > 100$ MeV/c there is plenty of signal in low transverse momentum bin but with the cut $p_T > 150$ MeV/c the signal practically disappear. Thus the low momentum cut was set at $p_T > 100$ MeV/c. The high transverse momentum cut was set at $p_T < 2$ GeV/c and this cut have little influence on the final signal.

The distribution of the transverse momentum is shown for positive and negative tracks separately in Fig. 4.11 with the selected region marked as shaded.

4.5.3 Track cuts efficiency

The Fig. 4.12 shows diagrams of the cuts efficiency, the right column for positive and the left for negative particles. The numbers are essentially the same. Most of the tracks are removed due to the cut on the fiducial volume in the polar angle. The next important cut is on the number of fitted hits. Overall around 42 % of all tracks are removed.

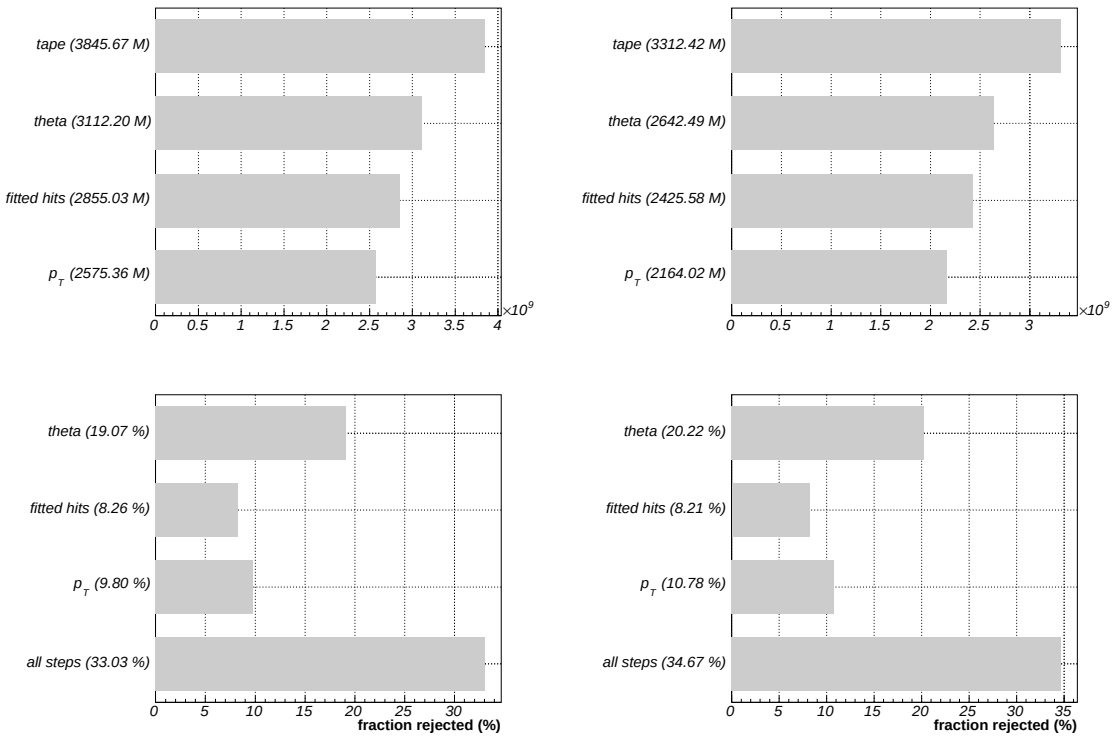

Figure 4.12: Number of tracks passing quality cuts

4.6 Invariant mass spectrum

For every pair of a positive and a negative track a 4-vector can be calculated representing the sum of the two vectors:

$$\begin{aligned} E &= E_1 + E_2 \\ p &= p_1 + p_2 \end{aligned} \tag{4.9}$$

where the p_1 and p_2 are the measured momentum 3-vectors of the incoming particles and E_1 and E_2 are calculated energies $E = \sqrt{m_0 + p^2}$, and m_0 is the pion rest mass. From the components of the 4-vector – (E, p_x, p_y, p_z) one can calculate invariant mass, transverse momentum and rapidity of the primary particle:

$$m_{\pi\pi} = \sqrt{E^2 - p^2} \tag{4.10}$$

$$p_T = \sqrt{p_x^2 + p_y^2} \tag{4.11}$$

$$y = \frac{1}{2} \log \left(\frac{E + p_z}{E - p_z} \right). \tag{4.12}$$

Most of the pairs are random combinations and only a small fraction comes from the K_S^0. These pairs shall be visible as a peak in the invariant mass spectrum.

The distribution of the invariant mass is shown in Fig. 4.13. The spectrum starts at mass twice of the pion mass and rises sharply up to $m \simeq 0.35$ GeV and then falls slowly. The signal of the K_S^0 is too weak in comparison with the combinatorial background to be visible.

To observe a signal an estimation of the combinatorial background have to be created. This is done using the event mixing procedure. The simplest implementation of the event mixing procedure is the following:

- the events are grouped into pairs, every odd event (n) is match with the next event $(n+1)$
- four sets of track pairs are created:
  - same events – $N_n \times P_n$, $N_{n+1} \times P_{n+1}$
  - mixed events – $N_n \times P_{n+1}$ and $N_{n+1} \times P_n$, where N_n stands for a set of all negative tracks in the n-th event and P_n for a set of positive tracks in n-th event.

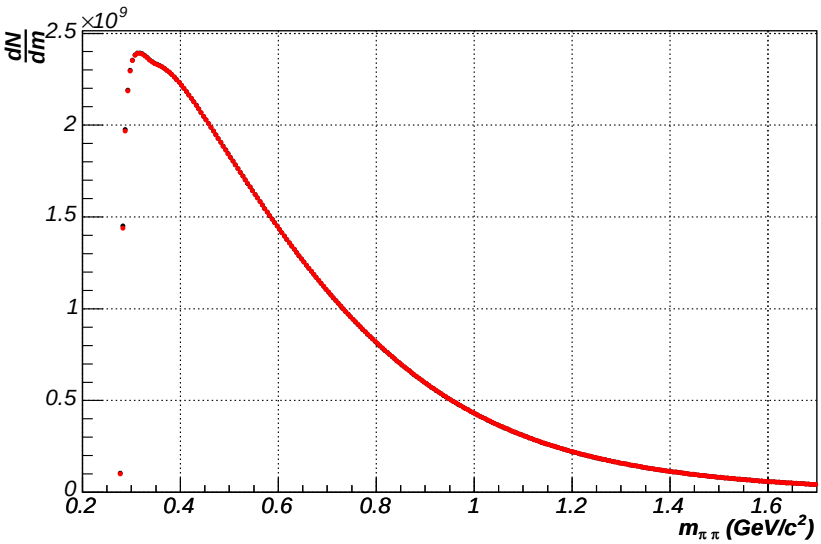

Figure 4.13: Invariant mass spectrum. Red points: same events, black points: mixed events scaled to match in integral.

The ratio of thus created spectra shall be equal to unity, except for the signal of the decaying particles, among them K^0_S. The real distribution presents a more complicated structure and it is shown in the first panel in Fig. 4.14, after subtracting the unity. The mixed events were scaled by a factor of 1.0293 to match the same events spectra in the integral, the origin of the difference in the number of pairs will be discussed below.

The distribution have a characteristic U–shape with the minimum around $m \simeq 0.9$ GeV/c^2. The variation of the ratio is on the level of $2 * 10^{-3}$. Three peaks are visible: the K^0_S peak at the position $m_{\pi\pi} \simeq 0.5$ GeV at the level of 10^{-3} and additionally a narrow peak at $m \sim 0.35$ GeV and a broad and weak peak at $m \simeq 0.7$ GeV. Those additional peaks can be due to additional particles eg. Λ, conversions or they can be connected with the variation of the background.

The next panels shows the difference between invariant mass spectra of same and mixed events – the signal. A clear peak of K^0_S is visible. The high signal at very low $m_{\pi\pi}$ can be attributed to conversions. The same plots of ratio and difference are repeated in the next row, focused on the region of interest.

The signal of the K^0_S is visible, but extracting it from the spectrum presented here with the precisions greater that $20-30\%$ is practically impossible. The simple method of event mixing gave an estimation of the combinatorial background precise enough to observe the signal, but to extract the yield of the K^0_S an order of magnitude more precise estimation is needed.

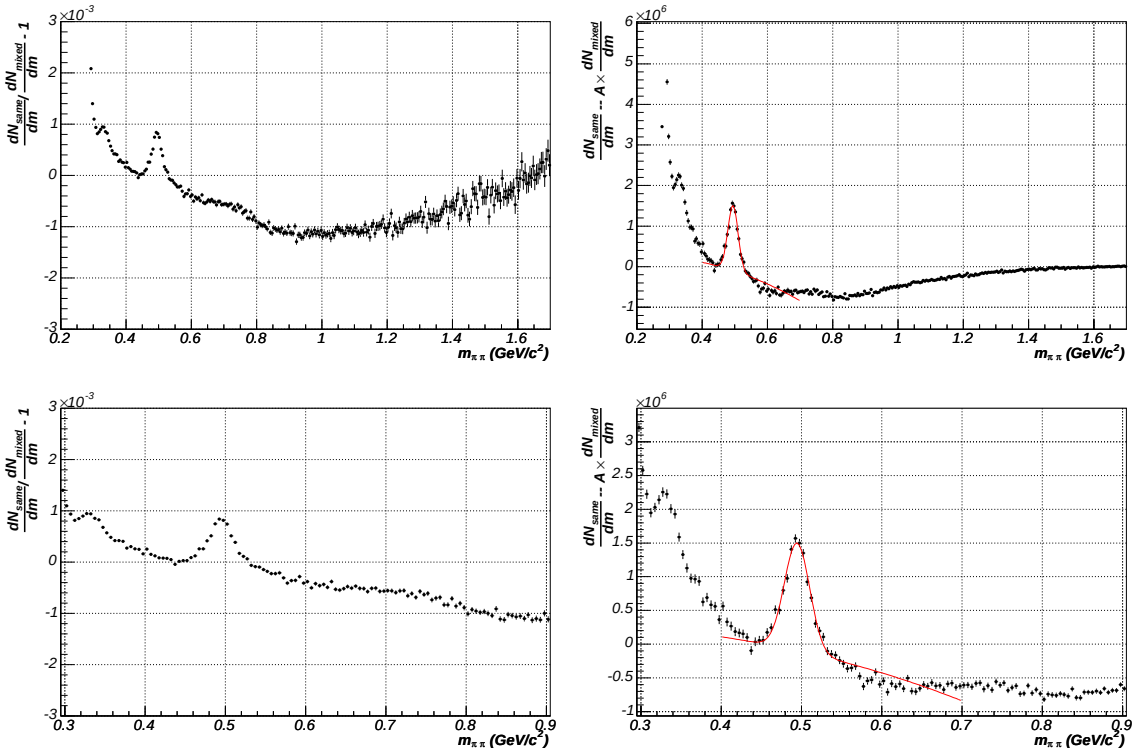

Figure 4.14: Invariant mass spectra. Top left: ratio of same to scaled mixed events with the unity subtracted, Top right: mixed events subtracted from same events. Bottom row: the same data zoomed on the region of K^0_S.

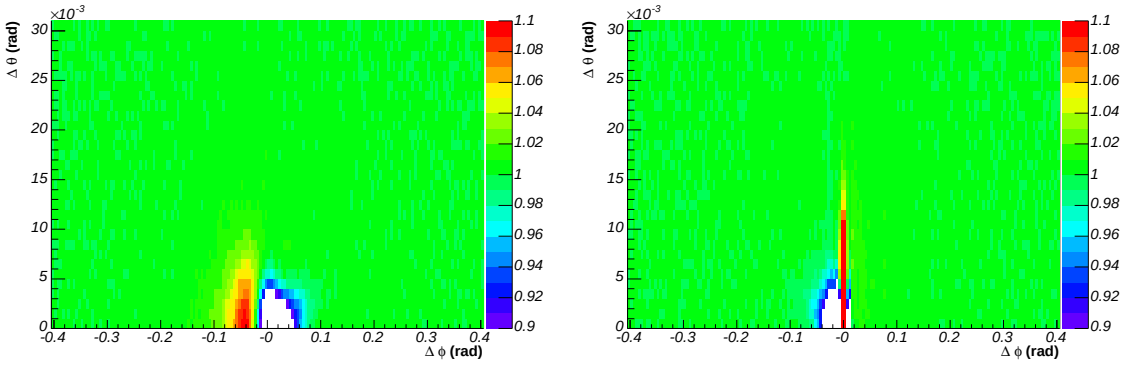

Figure 4.15: Small opening angle effects. Ratio of the distribution of $(\Delta\phi, \Delta\theta)$ of pairs in same over mixed events. Left panel: using ϕ_{R2M}, right panel: using $\phi_{firstHit}$

It can be expected that three sources of correlations contribute to the difference between shape of the invariant mass spectrum for same and mixed events. The first source is due to global correlations like azimuthal flow or momentum – multiplicity correlation. Second source is the contamination of the sample by misidentified weak decays, for example Λs. The third source are the detector effects like conversions $\gamma \rightarrow e^+e^-$ and double track resolution. The two have different physics origins, but experimentally are observed in the same region at low opening angles.

The discussion of the contribution of different effects will start with double track resolution and small opening angle effects. Then the correlation between momentum and multiplicity will be discussed. After the global correlations, the contamination of the kaon sample with misidentified Λ will be studied.

4.7 Double track resolution

The distribution of the invariant mass have a strong excess of pairs in same events with the mass close to the threshold. This suggests some phenomena in low opening angle develops.

The distribution of the opening angle can be decomposed into difference in the azimuthal $(\Delta\phi)$ polar angle $(\Delta\theta)$. The difference is measured from positive to negative track. The ratio of two-dimensional distributions of $(\Delta\phi, \Delta\theta)$ for same and mixed events is shown in Fig. 4.15.

The hole in the resulting distribution, at small angles, is due to finite double track resolution. Two topologies are possible for a pair of tracks of opposite charge: the field can bring the tracks closer (cowboy) or away (sailor). This effect is visible as an asymmetry

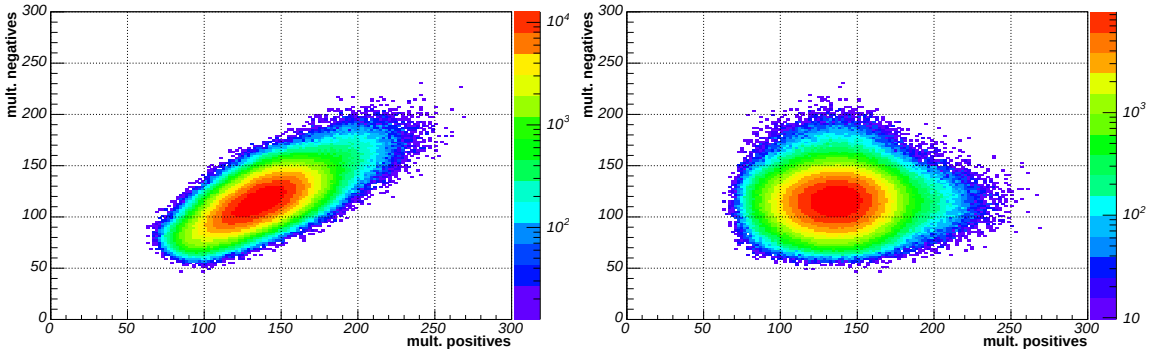

Figure 4.16: Correlation of multiplicity of positive and negative particles. Left panel: same events, right panel: mixed events

of the hole with respect to $\Delta\phi = 0$. The excess of pairs with small $\Delta\psi$ is visible for the sailor topology and is caused by the conversions.

For study of the low opening angle effects a $\phi_{firstHit}$ is a usefully variable. On the plot showing data using $\phi_{firstHit}$ one can observe that the tracks from the conversions tend to share the same first hit in the TPC.

The data show a rich structure at low opening angle. Since the kaons open appreciably in the CERES setup, with the opening angle for bulk of kaons $\psi \sim 0.2$ rad a safe cut can be placed at $\psi > 0.1$ rad. The cut on opening angle is order of magnitude greater that the double track resolution. The priorities to define the cut is the shape of the invariant mass spectrum.

4.8 Multiplicity correlation

The invariant mass spectra from same and mixed events differ in the total number of entries. The mixed events spectrum was scaled by a factor of 1.0293 to match the number of pairs in the spectrum of same events. The integral is different, due to correlation of the multiplicity of the positive and negative tracks in same events.

The distribution of the multiplicity of positives versus negatives in same events is shown in the left panel of Fig. 4.16, where a clear correlation is visible. In mixed events the correlation is absent as illustrated on the right panel in Fig. 4.16. The correlation in the multiplicity explains the difference in the total number of pairs.

If the momentum of tracks would not be correlated with the multiplicity, this would influence only the normalization but not the shape. Physical intuition suggests, the more

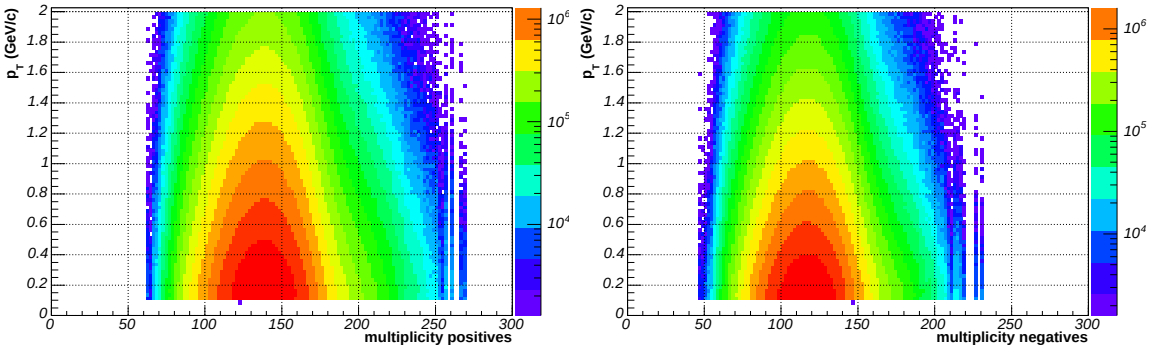

Figure 4.17: Correlation between momentum and multiplicity. Left panel: positive tracks, right panel: negative tracks.

energy is dissipated the more tracks are created and their mean energy is higher. This effect will produce a different shape of the invariant mass spectrum of same and mixed events. The correlation of the momentum of the tracks and the multiplicity is show in Fig. 4.17. The left panel shows positive tracks and the right negatives. In the plot each track is histogramed with x coordinate equal to the multiplicity of the event and y coordinate equal to the transverse momentum of the track.

In such representation the shape is dominated by the multiplicity and transverse momentum distribution, but not by the correlation between them. To avoid this problem and highlight the correlations the distribution can be divided by a product of the marginal distributions:

$$c(M, p_T) = \frac{f(M, p_T)}{g(M) * h(p_T)} \tag{4.13}$$

where the $f(M, p_T)$ is the distribution to be analyzed, in this case histograms shown in Fig. 4.17, dependent on multiplicity M and transverse momentum p_T. The marginal distributions:

$$g(M) = \int dp_T \, f(M, p_T) \tag{4.14}$$

$$h(p_T) = \int dM \, f(M, p_T) \tag{4.15}$$

are constructed by integration of the analyzed distribution. The resulting marginal distribution $h(p_T)$ is the transverse momentum distribution, and the $g(M)$ is a function of the multiplicity distribution. The correlation function $c(M, p_T)$ shall be equal to unity if two parameters are not correlated. In case of correlations, they will be visible as a departure

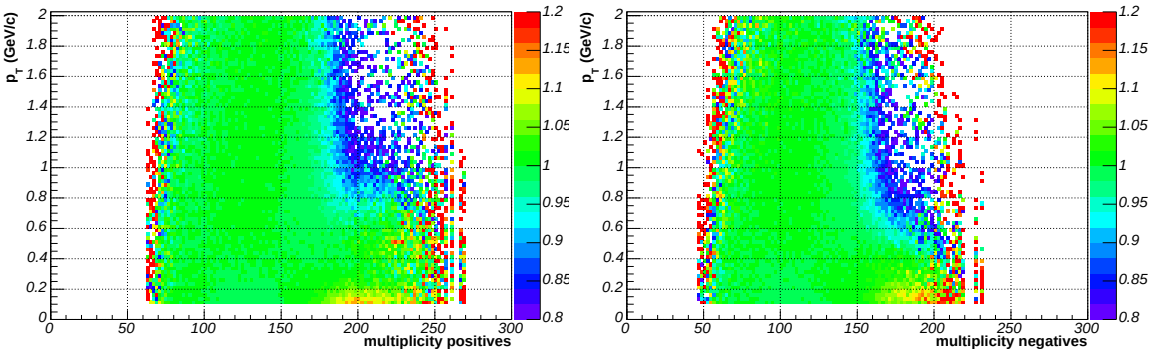

Figure 4.18: Correlation between multiplicity and transverse momentum. Left panel: positive particles, right panel: negative particles.

from the unity. If the hypothesis of the momentum dependence on the multiplicity is correct, then the left-bottom and the right-upper corners of the distribution will be above the unity and the opposite corners below.

The correlation functions are shown in Fig. 4.18, the left panel for positive and the right for negative tracks. A different structure as expected is visible. For low and medium multiplicity events the distribution is flat in the range of the statistics. For high multiplicity events a clear correlation develops. There are events with high multiplicity of either positive or negative tracks with significant excess of low momentum tracks and without high momentum tracks.

These events have to be classified as pathological. The events looks like low multiplicity events overlapped with the shower of the low momentum tracks. However, the physical source of the excess is not clear. Note that the events passed number of quality cuts which implies the trigger, centrality and total multiplicity in the TPC are as for good events. The events will be removed from the sample. The removal can not be included into the event cuts discussed in previous section, because the cut depends on the track cuts which are applied after event cuts.

For the clear estimation of the position of the cut the multiplicity distribution of positives and negatives was created and is shown in Fig. 4.19. The shape follows a Gaussian fit and for the large multiplicities an excess develops. In principle, the multiplicity do not have to be Gaussian, but since in the same region as departure from the Gaussian shape starts the excess of low momentum tracks is observed.

This cut will remove also the real, high multiplicity events. Assuming the number of real events follows Gaussian distribution, in the region where the shoulder develops, the number of events is already two decades smaller than typical events. Thus the cut will

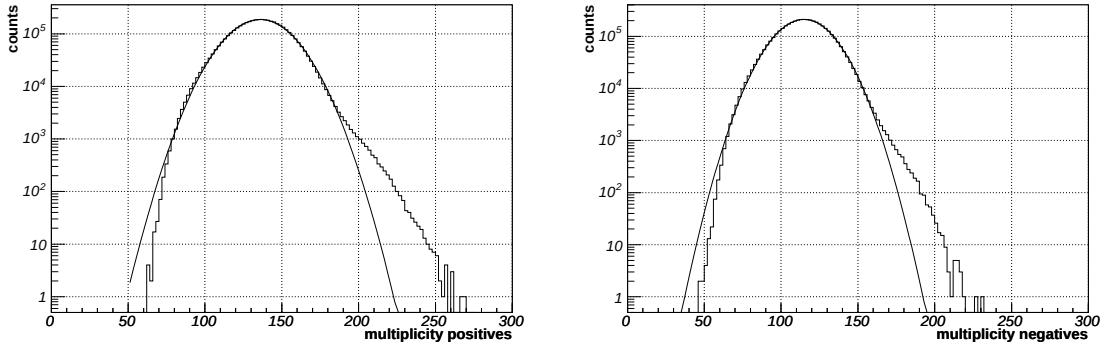

Figure 4.19: Multiplicity distribution of positives (left) and negatives (right) tracks.

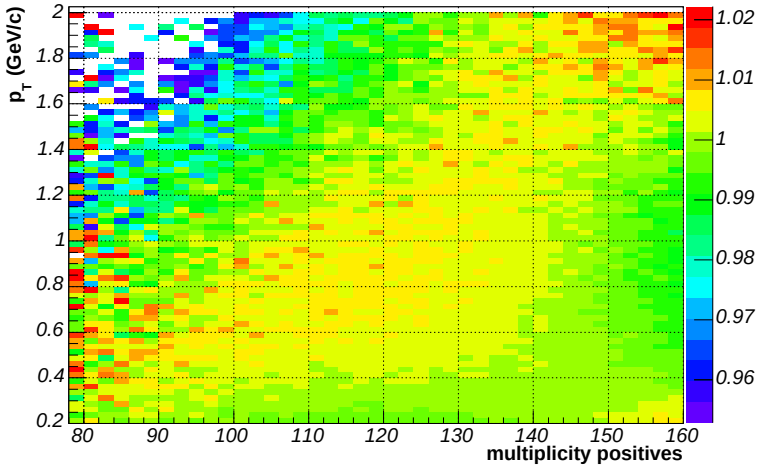

Figure 4.20: Multiplicity – momentum correlation for positive tracks

not significantly bias the sample.

The cut discussed does not solve the original problem of the multiplicity – momentum correlation. The same distribution as in Fig. 4.18, after the discussed cuts, is repeated in Fig. 4.20. Here the correlation as suggested by intuitive picture is visible.

4.9 Global correlations and event mixing

The previous, reference implementation of the mixing procedure (mixing with the next event) have to be modified to remove global correlation.

The new algorithm starts with excluding the pathological events from the sample. After the clean-up, every event is checked for mixing against every other event in the array of

loaded events. The checking is for example difference in the multiplicity of the positive and negative tracks and difference in the azimuthal anisotropy space. The checking does not mean the two events will be mixed, it means they fulfill the criteria for mixing. During this stage every event fills a list of candidates for mixing and the more typical the event, the more candidates it will have.

Then the actual mixing starts. The mixing is exclusive, the event once selected can not be reused. How to fix pairs from the list of candidates is yet another issue. The simplest method is selecting the first possible, not occupied, candidate from the list. The other possibility is to start with those who have smallest number of candidates for mixing and loop to those which have the larges choice .

Some events will not be mixed due to either lack of initial candidates or because the candidates were used before. These events are not used to create the invariant mass spectrum same events either. This fact can bias the sample; however, it can be assumed, the events that did not found any similar event out of 6000 events are in some sense different, most probably pathological.

The method discussed above do not give a warranty, the closest event will be chosen for mixing, it gives only the warranty the one chosen will be close enough. Other option is to search for the most similar event for every event. This brings many problems like weighting the difference in the multiplicity and in the flow. This method was extensively tested, but since the results where not sufficient the method will not be discussed in great details.

To boost the statistics one can try to mix with more events, for example 10. This brings another problems: the cuts will have to be released, which mean the shape of the spectrum will suffer; also the events will have to have exactly 10 matching events and this will bring complication to the procedure.

Intuitively, the most obvious cut in the selection for mixing is using events from the same target. Surprisingly this cut does not help and is even harmfully. After the track cuts the events from different targets look the same, but reducing the available sample by a factor of 13 reduces the possible combinations and the cuts have to be significantly looser. Also the probability, the event will stay without any candidate event for mixing is increased.

In the final analysis four cuts were applied. The difference in the multiplicity, separately for positives and negatives lower than $\Delta M < 10$ and two cuts where placed on the azimuthal asymmetry as discussed in the next section.

4.9.1 Azimuthal asymmetry

The azimuthal flow is the leading global correlation present in heavy ions collisions, thus careful analysis have to be performed for the proper event mixing. The schematic picture of the semi-central collision along the longitudinal direction is show in Fig. 4.2.

The overlapping area is where the collision takes place and the strongly interacting system is created. Two important features are visible: the system created is asymmetric and the spectators are shadowing the system. The direction of the impact parameter vector is called the reaction plane, the direction parallel to the reaction plane is called in-plane and the perpendicular direction is called out-of-plane.

At low energies, at SIS and AGS, the shadowing by the spectators is dominant and more particles is emitted out-of-plane [33]. With higher energies at SPS [34] and at RHIC [35] the spectators disappear faster and the bigger pressure builds up in the system. The pressure pushes the particles in–plane direction. This effect is called elliptical flow and is most prominent at midrapidity.

From the elliptic flow one can not establish if the projectile approached the target from left or right. This can be established using the asymmetry of the spectators at high rapidities and this asymmetry is called directed flow.

The concepts can be accommodated by decomposing the azimuthal distribution into Fourier coefficients [36]. The asymmetry of the event is analyzed by presenting a three dimensional distribution of the particles in rapidity, transverse momentum and azimuth:

$$E\frac{d^3N}{d^3p} = \frac{1}{2\pi}\frac{d^2N}{p_T dp_T dy}\left(1 + \sum_{1}^{\inf} 2v_n \cos\left(n\left(\phi - \Psi\right)\right)\right) \tag{4.16}$$

where E is the energy, p is the momentum vector, $\frac{d^2N}{p_T dp_T dy}$ is the two dimensional distribution in the rapidity – transverse momentum space, v_n are the Fourier coefficients for the azimuth ϕ, and Ψ is the event plane.

It is convenient to present the equation in a simpler form, dropping the dependence on the rapidity and transverse momentum:

$$\frac{dN}{d\phi} = 2v_1 \cos\left(\phi - \Psi\right) + 2v_2 \cos\left(2\left(\phi - \Psi\right)\right). \tag{4.17}$$

In principle every distribution can be described by an infinite number of coefficients. The experiment and the physical picture shows that the two terms are sufficient for description of the particles created during heavy ion collisions. At midrapidity where directed flow

vanish due to symmetry reason only the elliptic flow is present. Higher orders are not visible in the SPS data mostly due to low multiplicity.

The reaction plane is a line connecting centers of two nuclei. It is estimated by the event plane, which reflects the asymmetry of the produced particles. The event plane can be estimated in the following way:

$$X_n = \sum_i w_i \cos(n\phi_i) \tag{4.18}$$

$$Y_n = \sum_i w \sin(n\phi_i) \tag{4.19}$$

where the sum runs over all tracks in a given event with X_n and Y_n representing the total momentum in a given direction for the nth harmonic. The weights w_i are used to boost the signal. For elliptic flow, rising with transverse momentum, more information about the reaction plane is in the high–p_T tracks, so the weights are assigned to $w_i = p_T$. For directed flow the information is away from midrapidity.

With the total momentum in both directions, two quantities with direct physical interpretation can be obtained, :

$$\Psi_n = \frac{1}{n} \arctan\left(\frac{Y_n}{X_n}\right) \tag{4.20}$$

$$v_n = \frac{1}{M}\sqrt{X_n^2 + Y_n^2} \tag{4.21}$$

where Ψ is the event plane being the approximation of the reaction plane, v_n is the strength of the flow and M is the multiplicity. Studying the systematic of the elliptic flow as a function of beam energy, centrality, rapidity and the transverse momentum can yield interesting information about collective behavior of the system created. The measured value can be accommodated using hydrodynamical calculations [37, 38] or recently coalescence model [38].

These results, although very interesting by themselves, are not of importance for the study of the production of neutral strange mesons. The important message is, the events contain global correlation and while the events are mixed, these have to be taken into account.

For the rapidity range discussed, only the elliptical flow is of importance. The intuition suggests, the event for mixing shall have the same event plane angle and the same value of v_2. This method have some drawbacks. The first is theoretical, when the collision is very

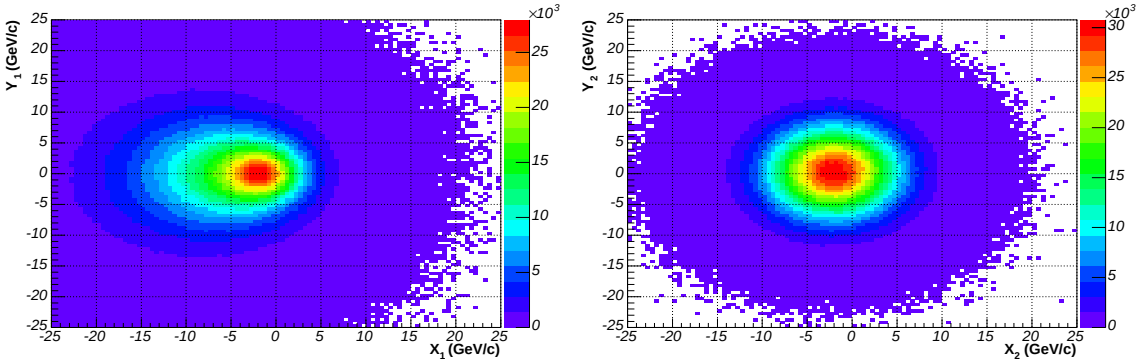

Figure 4.21: Total momentum asymmetry, left panel: directed flow, right panel: elliptical flow

central, there is little flow and thus the reconstruction of the event plane is mathematically an ill defined problem – the result is dominated by the fluctuations. Two central events, without flow can have opposite event planes even if they are in fact very similar. The second drawback is experimental. Beside the asymmetry from the elliptical flow there are additional asymmetries introduced by the detector, for example one chamber has smaller efficiency.

The distribution of the total momentum (X_1, Y_1) and (X_2, Y_2) are shown in Fig. 4.21. The distribution of the total momentum is not symmetric and the maximum for both cases is shifted from the origin of the coordinate system. Note that the distribution of the particles in one event is asymmetric due to flow but the distribution of the event plane have to be symmetric. If one aim at the flow analysis the distributions have to be calibrated before event plane and coefficients can be extracted. For our needs the plots only encourage to work directly on the total momentum space, not on the coefficients and the event plane angle. In short one works on asymmetries not on the hydrodynamical properties of the system created during heavy ion collision.

Finally in the actual analysis of K^0_S the following cuts where applied:

- elliptic flow: $\Delta(X_2,Y_2) < 5$ GeV/c
- directed flow: $\Delta(X_1,Y_1) < 15$ GeV/c

4.10 Armenteros-Podolanski space

The events contain true correlations, besides K^0_S, and even for the perfect method of event mixing the shape of the invariant mass spectrum of same and mixed events will differ. For

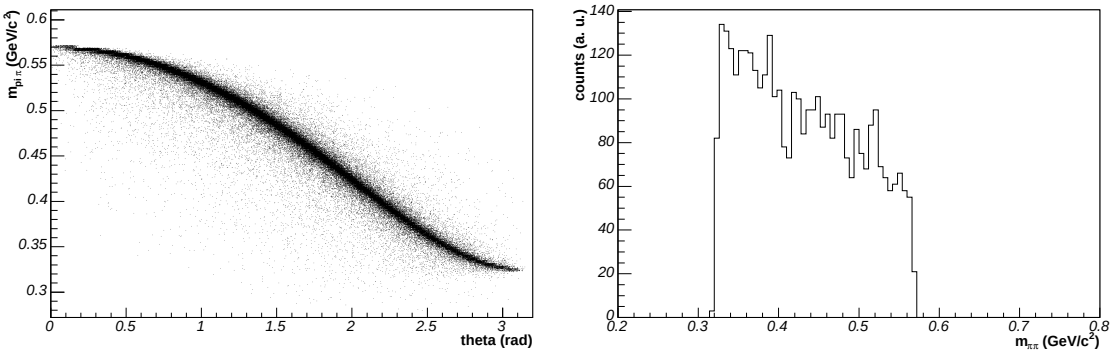

Figure 4.22: Invariant mass spectrum of the Λ misidentified for K^0_S. Left: invariant mass vs. polar angle of the proton. Right: mass spectrum of the Λs in the CERES acceptance.

example, the decay $\Lambda \to p\pi$ produces two correlated tracks. Since no particle identification is performed these correlations are visible in the $\pi^+\pi^-$ invariant mass spectrum.

The invariant mass expressed using momentum p and rest mass m of of two daughter particles is:

$$m^2 = m_1^2 + m_2^2 + 2\sqrt{m_1^2 + p_1^2}\sqrt{m_2^2 + p_2^2} - 2p_1p_2. \tag{4.22}$$

Since no particle identification is performed, the rest mass of daughters is not measured but assumed to the pions mass. The Λ particle, when reconstructed with the hypothesis of two pions, has different mass and this mass can be similar to that of K^0_S.

Lets consider a true Λ decaying into the proton and the pion, with the proton misidentified for a positive pion. When decay is considered in the center of momentum, the reconstructed invariant mass is $m = 0.34$ GeV/c^2. This mass is independent on the orientation of the decay. When the system is boosted to the lab frame the proton will gain more momentum than if it were pion. The reconstructed mass depends on the orientation of the proton with respect to the boost. The reconstructed invariant mass as a function of the polar angle with respect to the mother particle is shown in the left panel in Fig. 4.22. The highest mass is when the proton is emitted in a direction of the original track ($\theta = 0$ rad.) and the lowest when the proton is emitted backward. The distribution of the Λ invariant mass using $\pi^+\pi^-$ hypothesis in the CERES setup is shown in the right panel in Fig. 4.22. The high invariant mass part is suppressed, because when the pion is emitted backward, it has a very low transverse momentum and does not fall into the acceptance.

The signal of K^0_S can be cleaned from Λs using veto on the Λ hypothesis. The invariant mass is reconstructed assuming negative track is a pion and the positive is either a pion (K^0_S hypothesis) or a proton (Λ hypothesis). If the invariant mass of the Λ hypothesis is inside the expected Λ peak the invariant mass from the K^0_S hypothesis is not used.

Another possibility is the method developed by Armenteros and Podolanski. And described in Ref. [39]. The orientation of the decay with respect to the momentum vector of the mother particle is described using two variables: q_T and α.

The scalar variable q_T represents the transverse momentum of the positive particle with momentum vector p_+ with respect to the mother particle with momentum vector p_M:

$$q_T = \frac{|p_+ \times p_M|}{|p_M|}. \tag{4.23}$$

The variable α measures the asymmetry in the longitudinal direction with respect to the mother particle:

$$\alpha = \frac{q^+_L - q^-_L}{q^+_L + q^-_L} \tag{4.24}$$

where q^+_L is defined as a normalized scalar product of the momentum of the positive daughter and the mother:

$$q^+_L = \frac{|p_+ * p_M|}{|p_M|}. \tag{4.25}$$

The maximum of q_T is reached, when the daughter tracks goes transverse to the mother. In this case the $q_T = q$ (for K^0_S, $q = 209$ MeV/c [14]). In this configuration $\alpha = 0$. For symmetric particles, like two pions originating from the K^0_S, the decay shall be symmetric in α variable. This is not the case when the daughters differ in mass. In this case, since the heavier particle have higher momentum in the lab frame the center of the ellipse is shifted into direction of positive α for Λ of negative α for $\overline{\Lambda}$.

The Armenteros–Podolanski plot using CERES data is shown in the left panel in Fig. 4.23. Most of the pairs have $q_T \simeq 0.15$ GeV/c. The distribution is not symmetric with respect to the angle α, because there is more protons than anti-protons. In this representation the signal of kaons is not visible for the same reason it is not visible in the raw invariant mass distribution.

The K^0_S signal can be observed by constructing the difference of the two distributions. To highlight the correlations the distribution presented in the right side in Fig. 4.23

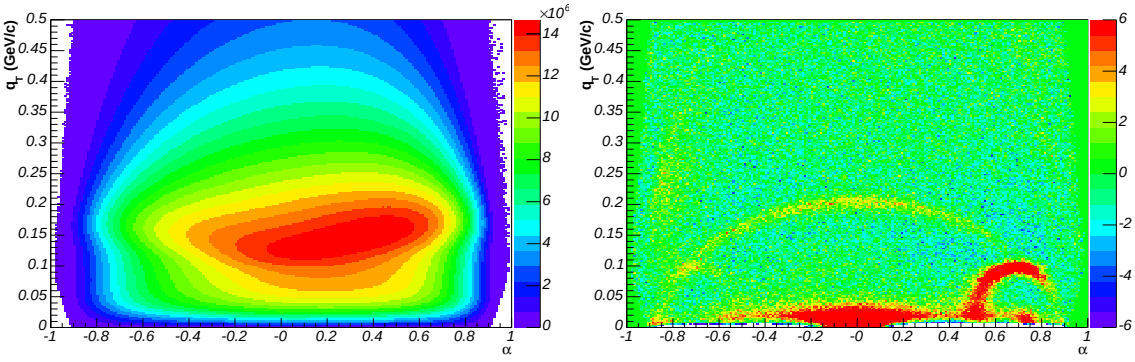

Figure 4.23: Armenteros-Podolanski plot. Same events (left) and the significance of the difference between same and mixed events (right)

shows pulls. The pulls are defined as a difference of two distributions normalized to the fluctuation of the background:

$$T(\alpha, q_T) = \frac{S(\alpha, q_T) - M(\alpha, q_T)}{\sqrt{S(\alpha, q_T)}} \tag{4.26}$$

where $S(\alpha, q_T)$ is the distribution for same events and $M(\alpha, q_T)$ for mixed events. The fluctuations of the background are $\sqrt{S(\alpha, q_T)}$.

A very rich structure of the correlations is visible. The correlation due to K^0_S is visible as an arc with q_T reaching $q_T = 0.209$ GeV/c. The arc is symmetric for $\alpha > 0$ and $\alpha < 0$. The correlation due to Λ is visible as and arc with center at $\alpha \simeq 0.7$ and momentum reaching $q_T \simeq 0.1$ GeV/c. On the opposite side of Λ the $\bar{\Lambda}$ is weakly visible.

Inside the Λ arc there is a correlation between proton and pion with the transverse momentum close to zero. This correlation is probably the pion–proton Coulomb interaction studied by the HBT methods.

The strong correlation symmetric with respect to $\alpha = 0$ and with small q_T is due to the conversions. And the absence of pairs with very small q_T and and $|\alpha| > 0.2$ is due to double track resolution. Additional correlations are visible with the origin not clear. These correlations can be due to the intrinsic transverse momentum fluctuations present in SPS data [40]. Some of these develop at $|\alpha| \simeq 0.8$, and cross the K^0_S line.

The cut in the Armenteros space is more powerful than the cut in the invariant mass hypothesis space. This have both advantages and disadvantages. The hypothesis cut is very gentle, it removes minimal fraction of the signal; however, this cut is difficult to reproduce in the simulation for the efficiency correction. The Armenteros cut removes

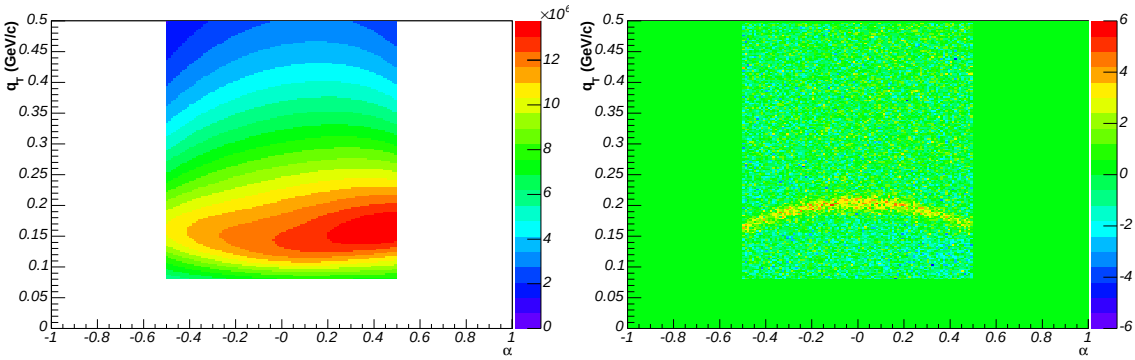

Figure 4.24: Armenteros-Podolanski plot after the cut.

almost 60% of the signal[1] but the cut is clean and, what is more important, with this cut also additional correlations can be removed. Actually the power of Armenteros cut to remove additional correlations was the driving factor in deciding where to place the cut.

The actually applied cut is shown in Fig. 4.24. With this cut, the hypothesis cut is not necessary. The figure shows that no major correlation develops in the considered area.

4.11 Invariant mass spectrum after cuts

The invariant mass spectrum after proper mixing and removal of residual correlations is shown on the left panel of Fig. 4.25. The right panel shown the ratio of same-to-mixed events with the unity subtracted. The ratio is flat and equal to zero in the mass region below the kaon peak and some correlations develop at masses higher to K^0_S.

The signal of the neutral kaons, constructed by subtracting the invariant mass spectrum for mixed events from same events, is shown in Fig. 4.26. The clear peak is placed on the flat noise. The presented spectrum was fit with Gaussian to guide the eye. Since the signal contains koans of different momentum the signal is not fully Gaussian.

In the mass region below the kaon peak the spectrum is clear of any correlations. In the mass region above the kaon peak some correlations are visible: a broad, weak peak. Its origin is not fully clear, one possible, experimental source can be residual multiplicity – momentum correlation. The broad peak can origin from short living, strongly decaying resonances. In Ref. [41] similar spectrum above the K^0_S mass was fit with the cocktail of ρ, ω and f_0 to extract their yields.

[1] For high transverse momentum koans, for the back-to-back topology at low momentum, the orientation in the Armenteros space is forced by the acceptance.

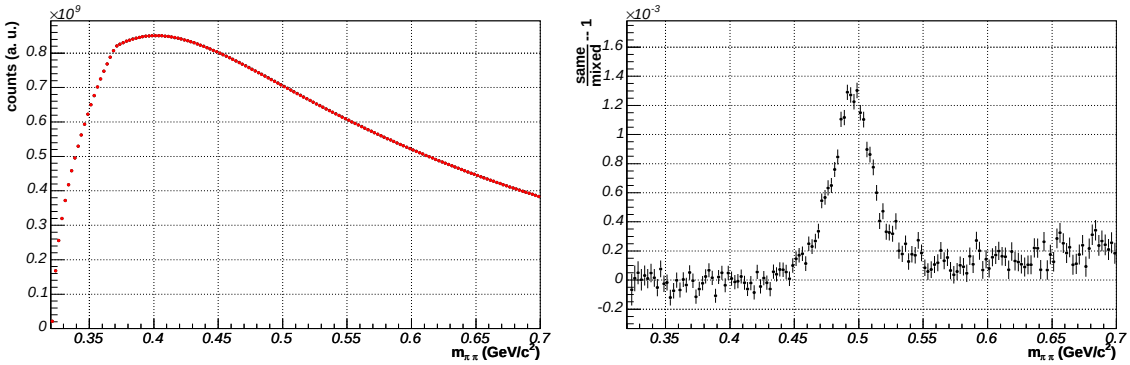

Figure 4.25: Invariant mass spectrum of $\pi^+\pi^-$ pairs. left: same and mixed events, right: ratio of same to mixed events after subtracting the unity.

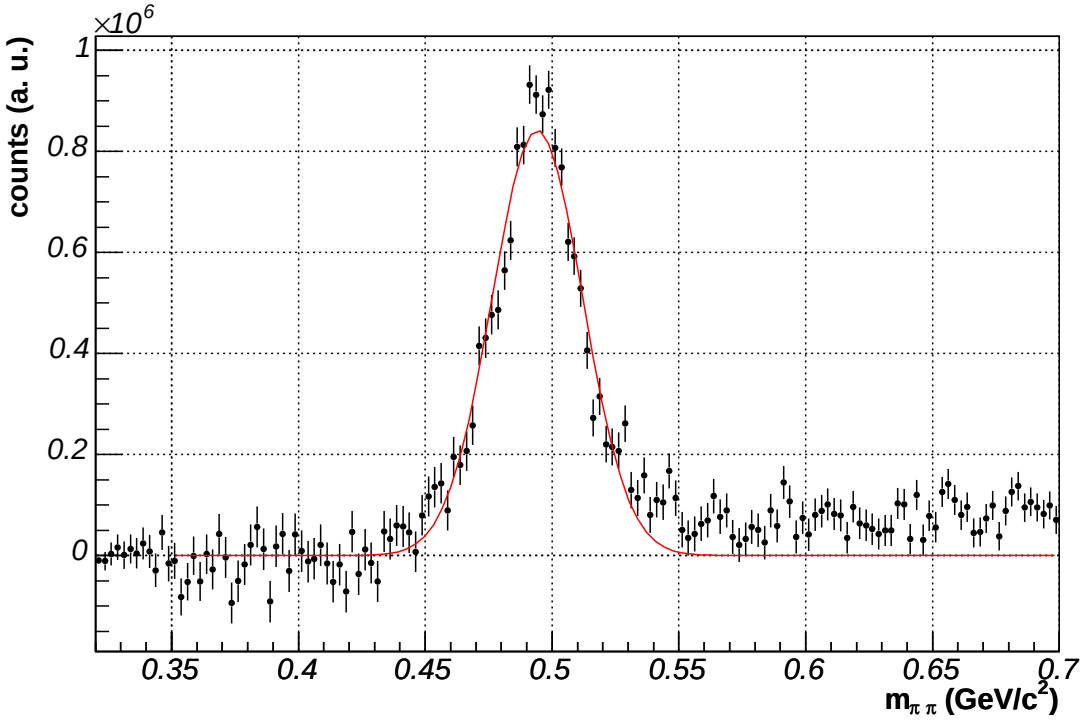

Figure 4.26: Invariant mass spectrum of this signal of the K^0_S. The spectrum is fit with the Gaussian to guide the eye.

With the invariant mass clear of residual correlations, distorting the extraction of the K^0_S, three steps have to be made to obtain a transverse momentum spectrum. The first step, described in the next chapter is the study of the reconstruction efficiency using Monte-Carlo simulation. Two following steps are described in Chapter 6 extraction of the kaon peak and finally the combination of the data with the results of the simulations.